1
Introduction to Magnetic Oxides

J. M. D. Coey, M. Venkatesan, and Hongjun Xu

Oxides are ubiquitous. The Earth's crust and mantle are largely made up of compounds of metal cations and oxygen anions. Looking at the composition of the crust in Figure 1.1, we see that oxygen is the most abundant element and the most common metals are aluminum and silicon. Most rocks are therefore aluminosilicates. The next most abundant element, and the only transition metal other than titanium to feature among the top ten, which account for over 99% of the crust, is iron (Table 1.1). Remarkably, the same electronic configuration, $2p^6$, is shared by five of the top ten ions, which account for 92% of the atoms in the crust. Usually, only iron, with its two common charge configurations, Fe^{2+} ($3d^6$) and Fe^{3+} ($3d^5$), forms ions with a partially filled shell containing electrons of unpaired spin that exhibit a net *magnetic* moment. At 2.1 at. % (5.7 wt.%), iron is 40 times as abundant as all the other magnetic elements put together; the runners up – manganese, nickel, and cobalt – trail far behind.

For over 20 centuries, up until about 1740 [1], the only useful permanent magnets known to man were lodestones. These prized natural magnetic rocks were largely composed of impure *magnetite*, the black spinel-structure oxide Fe_3O_4 with a ferrimagnetic structure that had been magnetized by a fortuitous lightning strike [2]. The other common rock-forming iron oxide is *hematite*, the reddish corundum-structure sesquioxide αFe_2O_3. Hematite is also magnetically ordered, in a canted antiferromagnetic structure, but its magnetization is about 200 times weaker than that of magnetite.

The weak remanent magnetism imparted to rocks as they cooled in the Earth's magnetic field has allowed us to read the record of fluctuations of the magnitude and direction of the field at the Earth's surface. The remanence is largely due to segregated nano crystallites of titanomagnetite in the rock [3]. The Earth's field is a precious shield that has protected us from the solar wind and allowed life to develop on our planet over the past 3.5 billion years. We learn from the magnetic record that it has reversed numerous times on a geological timescale. The tectonic movements of the plates were thereby pieced together, leading to the first unified theory of Earth sciences. It was actually a quest to understand the magnetism of rocks and baked clay that motivated Louis Néel to formulate the molecular field theory of ferrimagnetism [4], completing the theory of antiferromagnetism that

Functional Metal Oxides: New Science and Novel Applications, First Edition.
Edited by Satishchandra B. Ogale, Thirumalai V. Venkatesan, and Mark G. Blamire.

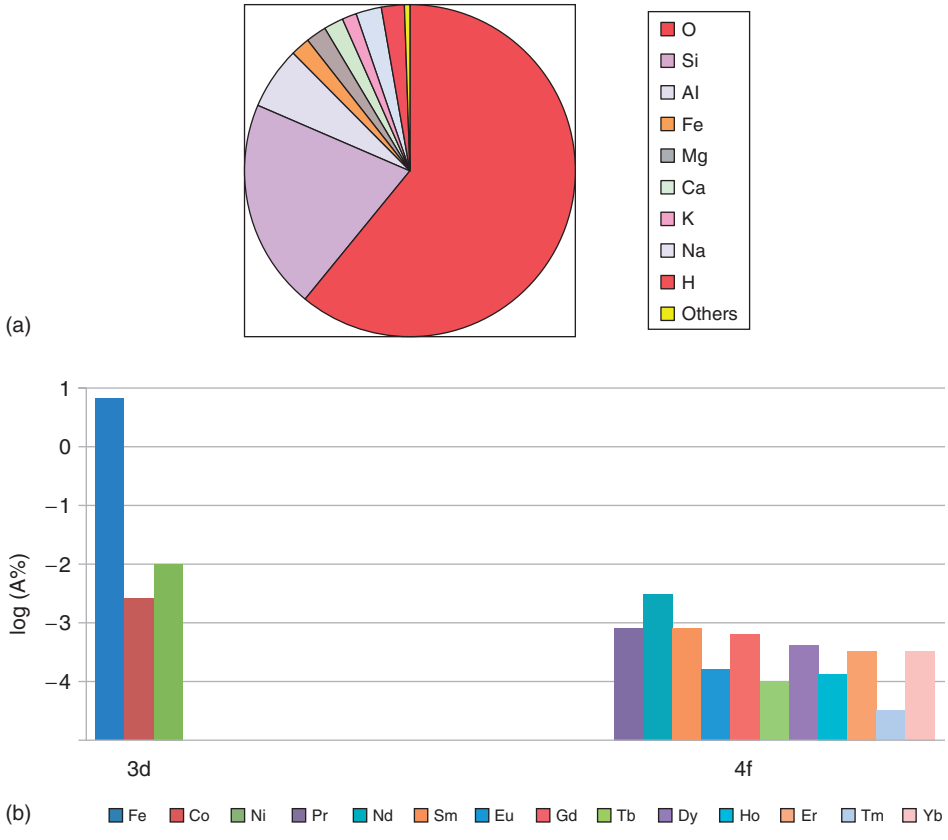

Figure 1.1 (a) Abundance of elements in the Earth's crust in atomic % and (b) abundance of magnetic elements.

Table 1.1 Elements in the Earth's crust (atomic %).

Ion	Abundance	Configuration
O^{2-}	60.7	$2p^6$
Si^{4+}	20.6	$2p^6$
Al^{3+}	6.1	$2p^6$
Na^{+}	2.6	$2p^6$
$Fe^{2+/3+}$	2.1	$3d^{6/5}$
H^{+}	2.1	$1s^0$ no electrons
Ca^{2+}	1.9	$3p^6$
Mg^{2+}	1.8	$2p^6$
K^{+}	1.5	$3p^6$
Ti^{4+}	0.3	$3p^6$

he had developed in his thesis, which was based on the original molecular field theory of ferromagnetism that his mentor and PhD supervisor Pierre Weiss had formulated in 1906, 30 years previously.

Ferrimagnetic oxides are quite strongly magnetic and insulating when the only iron ions they contain are ferric ions. This was a winning combination at the time because there was a need for magnetic materials to be used at microwave frequencies. Metallic alloys based on iron, or even magnetite itself (which contains both Fe^{2+} and Fe^{3+}), were unsuitable because of prohibitive eddy-current losses associated with their conductivity. Oxides from the cubic structural families of spinels and garnets, especially nickel–zinc ferrite, manganese–zinc ferrite, and yttrium–iron garnet (YIG), proved to be the champions here.

Another winning combination was ferrimagnetism and strong uniaxial anisotropy. This was the basis of the success of the hexagonal ferrites with the magnetoplumbite structure, which now account for 90% of the tonnage of permanent magnets produced worldwide. Discovered at the Philips laboratory in the Netherlands around 1950, these were the first true permanent magnets, in the sense that their coercivity could exceed their magnetization, which meant that they could remain magnetized whatever be their shape. A nice, square hysteresis loop is the icon of permanent magnetism. Individual magnet ownership has progressed from one or two per person 60 years ago to a 100 times as many today.

Magnetic recording, which demanded less permanently magnetized materials that could be remagnetized in the reverse direction, as required, spurred the next big development. This included the production of acicular (needlelike) particles of the other ferric sesquioxide, spinel-structure γFe_2O_3, which is known as *maghemite*. Subsequently, Fe_2O_3 was surface-doped with cobalt, and then acicular CrO_2, the only simple oxide that is a ferromagnetic metal was developed. These micrometer-sized particles made up the magnetic media on hard and floppy disks and tapes used for audio, video, and data recording for several decades. However, the relentless march of progress characterized by the magnetic version of Moore's law, which states that the areal density of recorded information doubles every 18–24 months, has now rendered particulate oxide media obsolete. Thin film metallic media are now used to store everything that is downloaded from the Internet..

Intellectually too, scientific interest in magnetic oxides has waxed and waned. The first Golden age was the 1950s and the 1960s, when the ferrites were explored and their properties optimized [5]. The phenomenology of the exchange interactions among localized electrons in 3d shells was systematically investigated [6]. Discovery of the first family of ferromagnetic oxides, the mixed-valence manganites, also dates from this period [7]. The interest in them revived when the copper oxide high-temperature superconductors were found to have a similar, perovskite-related structure, and the magnetoresistance of thin film mixed-valence manganites was shown to be ''colossal''. Ferromagnets have a higher magnetization than ferrimagnets, but the double-exchange mechanism that allows them to order magnetically above room temperature entails electrons hopping among localized cores ($3d^3$ for manganites and $3d^5$ for magnetite) so that the oxides are conducting and not insulating. The manganites illustrate nicely the progression from studies on bulk

ceramics to single crystals to thin films and other nanostructures which marks the historical evolution of research in magnetic oxides.

We may now be entering a new Silver age for oxide research, where multifunctionality, control of defects, interfaces, and thin-film device structures are the new challenges [8]. These ideas are discussed in the later chapters of the book. Here we do the groundwork, by introducing some of the basic ideas and magnitudes relating to structure and properties of magnetic oxides [9, 10]. SI units are used consistently throughout this chapter, but tables of cgs conversions can be found in textbooks on magnetism [11]. The merits of using SI units are compelling. Not only is it possible to check that equations are dimensionally correct, but ideas about the shape of $M(H)$ hysteresis loops, for example, clear when M and H are measured in the same units (ampere per meter).

1.1 Oxide Structures and Crystal Chemistry

Oxides are ionic compounds where small, highly charged metal cations are embedded in a lattice of oxygen anions. The O^{2-} has its stable $2p^6$ closed-shell configuration with an ionic radius $r_O = 140$ pm. Frequently the oxygen forms a dense-packed or distorted dense-packed lattice, either face-centered cubic (fcc) ABCABC or hexagonal close packed (hcp) ABABAB. There are two types of interstices in these structures, illustrated in Figure 1.2, which may be occupied by cations. The smaller one is the tetrahedral site with four oxygen neighbors, which can accommodate, without distortion, a spherical cation of radius $r_{tet} = ((3/2)^{1/2} - 1)r_O = 32$ pm. The

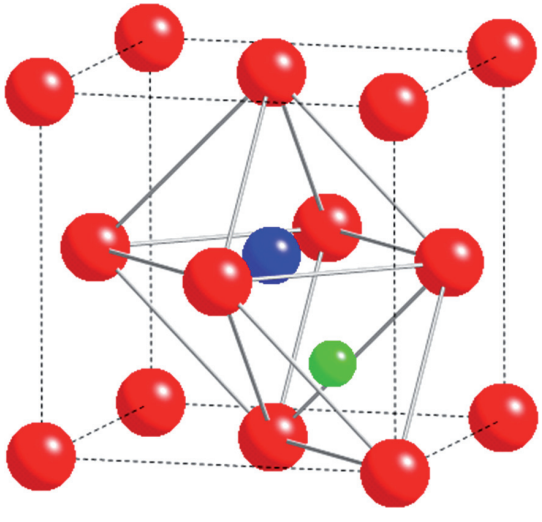

Figure 1.2 A close-packed oxygen lattice showing octahedral (blue) and tetrahedral (green) cation sites.

larger one is the octahedral site with six oxygen neighbors that can accommodate a spherical cation of radius $r_{oct} = ((2)^{1/2} - 1)r_O = 58$ pm. Here r_O is taken as 140 pm.

Table 1.2 lists the ionic radii of common 3d cations, and others that may be incorporated in oxide structures. All the tetrahedral and most of the octahedral cations create some distortion of the site. There are two tetrahedral interstices, and one octahedral interstice for each oxygen in dense-packed lattices; so that only a fraction of them can ever be filled. The larger cations such as Sr^{2+} or La^{3+} have ionic radii comparable to that of oxygen, and they often substitute for oxygen ions in the dense-packed lattice with a 12-fold oxygen coordination. The ionic radii of the trivalent rare earths in a 12-fold coordination decrease monotonically from 136 pm for La^{3+} to 114 pm for Lu^{3+}. Divalent Eu^{2+} has a stable half-filled shell $4f^7$ with $r = 140$ pm. Ionic radii increase with coordination number; they are about 25% smaller for the rare earths in 6-fold coordination than in a 12-fold coordination.

A variety of defects can be found in oxide structures [12]. Point defects include vacant oxygen or metal sites, and metal cations in interstitial sites, which are unoccupied in the perfectly-ordered structure. The former may trap one or two electrons, in which case the defect is known as an *F center*. Planar defects include grain boundaries in polycrystalline material, and missing planes of oxygens such as those found in the Magnéli phases Ti_nO_{2n-1}, which are based on rutile-structure TiO_2. Defects modify the electronic structure and may influence the optical and magnetic properties.

The ionic picture is, of course, an oversimplification. The chemical bond between metal and oxygen has part-ionic and part-covalent character, governed by the electronegativity of the atoms involved. The covalent character is more pronounced in tetrahedral sites and for cations (such as V^{4+}) with a high formal charge state.

Next we briefly present ten representative structures encountered in magnetic oxides. Of course there are many more than ten oxide structures, but these examples serve to illustrate the structural principles and cover the most common materials. We refer to them by the name of a mineral type, which is not necessarily an oxide. In each case a picture of the structure is included in Figure 1.3, and structural information on specific nonmagnetic oxides is provided in Table 1.3.

Table 1.2 Ionic radii of cations in oxides.

Fourfold tetrahedral	pm	Sixfold octahedral	pm	Sixfold octahedral	pm	12-fold substitutional	pm
Mg^{2+}	53	Cr^{4+} $3d^2$	55	Ti^{3+} $3d^1$	67	Ca^{2+}	134
Zn^{2+}	60	Mn^{4+} $3d^3$	53	V^{3+} $3d^2$	64	Sr^{2+}	144
Al^{3+}	42	Al^{3+} 54	—	Cr^{3+} $3d^3$	62	Ba^{2+}	161
Fe^{3+} $3d^5$	52	Mn^{2+} $3d^5$	83	Mn^{3+} $3d^4$	65	Pb^{2+}	149
Si^{4+}	40	Fe^{2+} $3d^6$	78 (61)	Fe^{3+} $3d^5$	64	Y^{3+}	119
—	—	Co^{2+} $3d^7$	75 (65)	Co^{3+} $3d^6$	61 (56)	La^{3+}	136
—	—	Ni^{2+} $3d^8$	69	Ni^{3+} $3d^7$	60	Gd^{3+} $4f^7$	122

Values in brackets indicate a low-spin state.

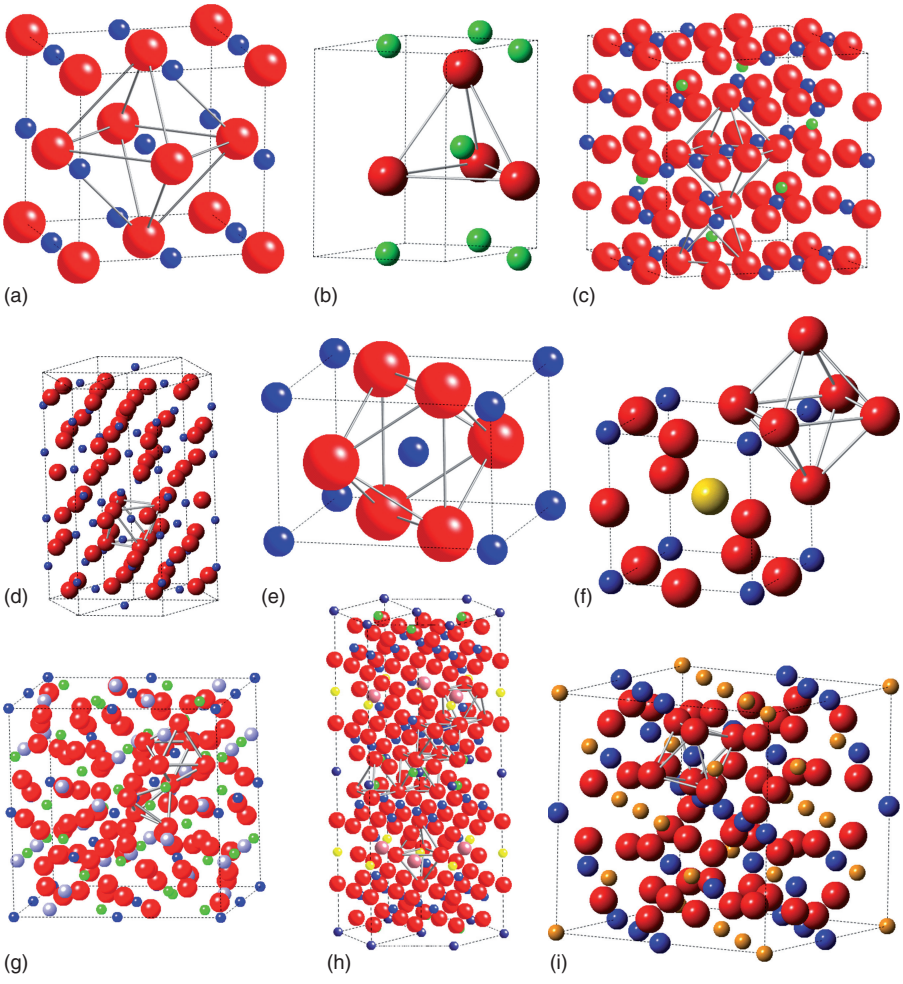

Figure 1.3 Some common oxide structure types (a) halite, (b) wurzite, (c) spinel, (d) corundum, (e) rutile, (f) perovskite, (g) garnet (h) magnetoplumbite, and (i) pyrochlore.

- *Halite*. The NaCl structure is composed of two interpenetrating fcc sublattices, with cations and anions alternating along [100] directions. Cations are octahedrally coordinated by anions and vice versa.
- *Wurzite*. The ZnS structure is composed of two interpenetrating hcp sublattices, so that cations and anions alternate along the 001 direction. Here the cations are tetrahedrally coordinated by anions and vice versa. The structure lacks a center of symmetry, and compounds with this structure may be piezoelectric or pyroelectric.
- *Spinel*. The structure of $MgAl_2O_4$ is based on an fcc array with 32 oxygen ions where $1/8$ of the tetrahedral interstices (A-sites) are occupied by Al and $1/2$ the octahedral interstices (B-sites) are occupied by a mixture of Mg and Al. This

Table 1.3 Properties of nonmagnetic oxides.

Compound	Structure	Lattice parameters (pm)	E_g (eV)	ε_0
MgO	Halite	$a_0 = 421$	7.8	9.7
ZnO	Wurzite	$a = 325$; $c = 521$	3.4	8.2
$MgAl_2O_4$	Spinel	$a_0 = 808$	5.6	8.6
Al_2O_3	Corundum	$a = 476$; $c = 1299$	8.8	10
TiO_2	Rutile	$a = 459$; $c = 294$	3.0	110

E_g is the energy gap and ε_0 is the dielectric constant.

is known as the *inverse cation distribution*. The lattice parameter is $a_0 = 808$ pm. The B-sites form a lattice of corner-sharing tetrahedra, which leads to frustration of antiferromagnetic superexchange in spinel ferrites with the normal cation distribution (Fe^{3+} on B-sites).

- *Corundum (sapphire)*. This structure of Al_2O_3 is based on an hcp oxygen array, where Al occupies $^2/_3$ of the octahedral interstices. The structure is rhombohedral, but it is often indexed on a larger hexagonal cell with 32 oxygen ions and $a = 476$ nm, $c = 1299$ nm.
- *Rutile*. This structure of TiO_2 can be regarded as a distorted hcp oxygen array, where Ti occupies $^1/_2$ of the octahedral interstices. Each hcp sheet is deformed into a centered cubic array; so the structure is tetragonal with just four oxygen ions in the unit cell and $a = 459$ pm, $c = 256$ pm. TiO_2 can also crystallize in the anatase structure.
- *Perovskite*. The $CaTiO_3$ structure is pseudocubic with $a_0 = 379$ pm. Here the Ca and O ions together form an fcc lattice, and the Ti ions occupy $^1/_4$ of the octahedral interstices, coordinated only by oxygen. The cell tends to be rhombohedrally or orthorhombically distorted, depending on the cation:oxygen radius ratios.
- *Double perovskite*. A variant of the perovskite structure has a unit cell doubled in all three directions, with 24 oxygen atoms. There are now two different octahedrally coordinated cations in the structure, which form a NaCl-type superlattice.
- *Garnet*. Pyrope, $Ca_3Fe_2Si_3O_{12}$, has a big cubic unit cell with $a_0 = 1145$ pm containing 96 oxygen atoms. The calcium is coordinated by eight oxygens; iron is in octahedral sites and silicon is in tetrahedral sites; $Y_3Fe_5O_{12}$ is known as YIG.
- *Magnetoplumbite*. $PbFe_{12}O_{19}$ has a tall hexagonal cell with $a = 589$ pm, $c = 2309$ pm, containing 76 oxygen ions. The structure can be considered as an hexagonal ABABAABABA stack of oxygen and lead ions, with the iron sites coordinated only by oxygen. There are three octahedral sites, a tetrahedral site and a five-coordinated trigonal bipyramidal site.
- *Pyrochlore*. This is a mineral with the ideal formula $Ca_2Nb_2O_7$. The structure is derived from that of fluorite (CaF_2), where the fluorine anions form a simple cubic array, with calcium in alternate body-centers, forming an fcc cation array. In pyrochlore, the lattice parameter is doubled, $^7/_8$ of the fluorine sites are occupied

by oxygen but 1/8 are vacant, and the structure includes an array of corner-sharing Ca tetrahedra. There are 56 oxygen ions in a cubic cell with $a_0 = 1008$ pm.

We conclude this section with a few remarks on the electronic structure of oxides. Normally, the oxides are insulators, with a valence band derived from the filled $2p^6$ oxygen levels, and a conduction band derived from unoccupied metal orbitals. Examples where no unpaired transition- element electrons are present are MgO, ZnO, $MgAl_2O_4$, Al_2O_3, and TiO_2. This is also a list of commonly-used substrates for thin-film growth of the magnetic counterparts. Properties of these baseline nonmagnetic oxides are given in Table 1.3. All have a wide bandgap and are optically transparent as single crystals and the powders are white.

Schematically, the electronic structure of the magnetic 3d metal oxides TO_x comprises a filled $2p^6$(O) valence band separated from a 4s(T) conduction band by a primary energy gap E_g of several electron volts. The occupied $3d^n$ level of the transition-metal ion may then lie in the gap, or else it may lie below the top of the 2p band, provided that the $3d^{n+1}$ level lies above the top of the band. The value of n defines the valence state of the cation. The cations at the beginning, middle, and end of the 3d series tend to be quadrivalent, trivalent, and divalent, forming dioxides, sesquioxides, and monoxides, respectively. Examples are TiO_2 ($n = 0$), Fe_2O_3 ($n = 5$), and NiO ($n = 8$). On progressing across the 3d series, the occupied 3d level moves from a position high in the gap to a position below the top of the 2p band, owing to the stabilizing effect of the increasing charge on the transition-metal nucleus. Moreover, d bands tend to become narrower on moving across the series for the same reason.

The structure more frequently encountered when a transition metal is present in the structure, is for the $3d^n$ level to fall in the gap. Narrow d bands are formed by 3d(M) – 2p(O) hybridization, which frequently leads to optical absorption in the visible – leading to the observed colors (red for hematite, green for YIG, and black for magnetite) [14].

When the 3d level lies in the gap and the energy of the excitation $2(d^n) \rightarrow d^{n-1} + d^{n+1}$ is less than the 3d or 4d bandwidth, the oxide is a d-*band metal*. Examples include CrO_2 and $SrRuO_3$. However, if the energy of this excitation exceeds the d bandwidth, the material may be a *Mott insulator*, but when $3d^n$ level lies below the top of the 2p band, the relevant low-energy electronic excitation is $p^6d^n \rightarrow p^5 + d^{n+1}$. According to whether this is less than or greater than the d bandwidth, the material is a p/d *metal* or a *charge-transfer insulator* [13] (Figure 1.4).

There are a few ferromagnetic metal oxides where the 3d bands are spin split to the extent that a spin gap appears in either the ↑ or ↓ subband, and the electrons at the Fermi level are completely spin-polarized. Such materials are known as *half metals*. Stoichiometric half-metals exhibit a spin moment per unit cell which is an integral number of Bohr magnetons.

Oxides may not be precisely stoichiometric, but small deviations often have little influence on the electronic properties because the electrons or holes create a distortion of the lattice, forming immobile polarons that have a large effective mass.

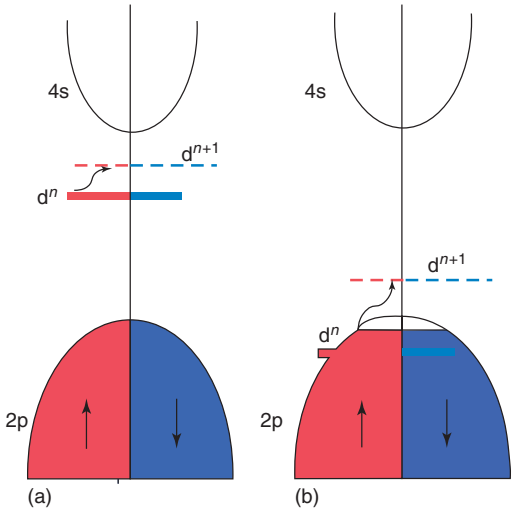

Figure 1.4 Electronic structure of a 3d oxide for an early transition metal (a) and a late transition metal (b). The low-energy d–d and p–d electronic excitations are shown.

1.2 Oxide Growth

1.2.1 Polycrystalline Materials

The easiest methods of oxide growth involve physical or chemical reactions that yield bulk polycrystalline material.

1.2.1.1 Precipitation

Precipitation is a widely used wet-chemical technique for synthesizing ultrafine ceramic powders of simple or complex oxides with a narrow particle size distribution [15]. The method avoids complex steps such as refluxing of alkoxides, and it is faster than other techniques. Precipitation or coprecipitation from aqueous salt solutions (nitrate, sulfate, chloride, perchlorate, etc.) by fine control of the pH by adding NaOH or NH_4OH solutions yields a poorly-crystallized hydroxide or an intimate mixture of the hydrated oxides. The particle size of the precipitate is strongly dependent on pH and the molarity of the precursor solution; it is usually converted to oxide by heating in air. The coprecipitation method offers simple and rapid preparation of complex oxides with control of particle size and good overall homogeneity.

1.2.1.2 Sol–Gel

The sol–gel method is based on the hydrolysis and condensation of metal–organic precursors in organic solvents [16]. The starting materials used in the preparation of the sol are usually inorganic metal salts or metal organic compounds such as

metal alkoxides $M(OR)_z$ where R is an alkyl radical ($R = CH_3$, C_2H_5, etc.). In a typical sol–gel process, the precursor is subjected to a series of hydrolysis and polymerization reactions to progressively form a colloidal suspension, known as the *sol*. Further processing leads to the *gel*, from which it possible to make materials in different forms such as ultrafine or spherical-shaped powders. Thin films are produced by dip coating. All are normally subject to post-deposition heat treatment.

1.2.1.3 **Solid-State Reaction**

Solid-state diffusion is often used to make complex oxides from an intimate mixture of microcrystalline precursor powders [17]. Neither a solvent medium nor controlled vapor-phase interactions are involved. Sometimes known as *shake 'n' bake*, it is the most widely used method for the preparation of complex oxides from a mixture of solid starting materials. Interdiffusion takes place at an appreciable rate at high pressure and/or high temperature (1000–1500 °C for several days). The rate of the solid-state reaction also depends on the ambient atmosphere, structural properties of the reactants, their surface area, reactivity, and the thermodynamic free energy change associated with the reaction. Several cycles of grinding the powder and refiring at progressively higher temperatures are usually necessary to achieve a pure phase. Solid-state synthesis is used to create ceramic powders or dense polycrystalline sintered masses. It may be advantageous to use precursors such as carbonates or oxalates, which decompose at low temperature to give fine-grained oxides.

1.2.1.4 **Combustion Synthesis**

The term covers a group of methods related to solid-state synthesis and coprecipitation where a fuel is incorporated in the mixture to be fired [18]. An exothermic reaction promotes uniform heating of the solid mass, and the production of oxide powders with a narrow crystallite size distribution in the range 10–100 nm. The solution method typically involves dissolving the precursors such as metal nitrates (the oxidizer) and a compound such as urea or glycine (the fuel) in water, followed by a self-sustaining reaction between the dried constituents, initiated at a relatively low temperature of 500 °C. Microwave irradiation may be used to modify the reaction conditions using a simple microwave oven.

1.2.2 **Single Crystals**

Single crystals, which may range in size from micrometers to centimeters, are needed for detailed characterization of the physical properties including the elementary excitations (magnons, phonons, and excitons). The key to growing them is control of the nucleation process.

1.2.2.1 **Bridgeman Method**

The Bridgeman method is a slow, controlled freezing process taking place under liquid–solid equilibrium conditions by allowing the solid–liquid interface to move

slowly until the entire molten charge is solidified [19, 20]. The growth takes place in a temperature gradient, and the idea is to create a single nucleus from which a single crystal will grow. The method involves melting polycrystalline material in a crucible with a pointed end and slowly cooling it from the bottom where a seed crystal nucleates at the tip. The crystal grows progressively up the length of the crucible. Either the crucible itself or a tube furnace with a temperature gradient can be moved. Compared to other growth methods, the Bridgeman method is rather simple but it cannot be applied if the system decomposes before it melts, or to oxides of elements with a high vapor pressure.

1.2.2.2 **Czochralski Method**

The Czochralski process is widely used to grow large single-crystal boules of semiconductors such as silicon, germanium, and gallium arsenide, but it can also be applied for many oxide crystals including Al_2O_3 (sapphire), $LaAlO_3$ (LAO), $Y_3Fe_5O_{12}$ (YIG), $Y_3Al_5O_{12}$ (YAG), and $Gd_3Ga_5O_{12}$ (GGG) [21]. Single-crystal material is pulled out of a slightly undercooled melt by dipping in a single-crystal seed and then slowly withdrawing it. The seed crystal rod is rotated at the same time as it is drawn out, and by precisely controlling the atmosphere, temperature gradient, rate of pulling, and speed of rotation, it is possible to extract a large, single-crystal oxide boule from the melt, which may then be sliced and polished to make substrates for thin film growth of other oxide materials.

1.2.2.3 **Zone Melting (Image Furnace)**

In the *float-zone* technique, the sample is in the form of a vertical polycrystalline rod, clamped only at its ends, a short segment of which is melted by a local heating [22]. The molten zone is suspended as a drop between the two solid parts of the rod, and it is moved along the rod by slow motion of either the heater or the rod itself. The optical floating zone technique, which makes use of an infrared image furnace, has been extensively utilized to grow single crystals of oxides. Early designs had one or two mirrors, but now, four mirrors are generally used to obtain more uniform sample heating. Ellipsoidal mirrors are used to focus the light from a halogen or xenon lamp onto the sample to produce the molten zone, making the technique suitable for both conducting and nonconducting materials. Optical heating is particularly convenient and efficient for oxides that absorb easily in the infrared. The sample is protected from its environment by a large diameter, clear quartz tube, which prevents evaporated material from settling on the mirror and allows control of the growth atmosphere and gas pressure around the growing crystal [23]. Optimizing crystallization rate, atmosphere, gas pressure, and temperature is the key to achieving stable growth and, good crystal quality. This technique is commonly used to produce pyrochlore, perovskite, and double-perovskite single crystals. Zone melting also helps to purify the oxide.

1.2.2.4 **Flux Method**

The flux method involves crystal growth by slow cooling of a high-temperature solution. It is suitable for growing crystals of incongruently-melting compounds,

but virtually any stable oxide may be grown from a suitable solvent. The flux and the oxide or its constituents are melted in a platinum crucible, which is then cooled extremely slowly. Times of order a month may be required to complete the crystal growth cycle. Oxides (B_2O_3, Bi_2O_3, BaO, and PbO), hydroxides (KOH and NaOH), or halides such as PbF_2 can be used as solvents [24]. However, eutectics, found in binary ($PbO-PbF_2$, Li_2O-MoO_3, $Li_2O-B_2O_3$, etc.) or ternary diagrams, are generally preferred owing to their low temperature of melting and low viscosity. Flux growth is useful whenever the melting temperature is high and when the vapour pressure at the melting point is elevated. The main disadvantage of the technique is the low-growth rate, more than 100 times slower than for crystals pulled from the melt. Crystals may take weeks to grow.

1.2.2.5 Chemical Vapor Reactions

Transport of material in the gas phase is used to grow crystals in a sealed quartz tube that is placed in a temperature gradient in a tube furnace [25]. A powder of the oxide to be grown is included with a transport agent such as I_2 or $TiCl_2$ with which it can react. When the reaction is exothermic, the oxide is transported from the cool zone of the furnace to the hot zone where the compound decomposes and the oxide crystals grow. The temperature gradient must be carefully controlled, and the process may take several days, but the quality of the small oxide crystals is often excellent.

1.2.3 Thin Films

Magnetic oxide thin films can be prepared by physical or chemical methods. In physical deposition methods, a source of material is separated by a distance d from the substrate, which is often heated in the range 400–1000 °C to facilitate growth [26]. Some variants are indicated in Figure 1.5. At low pressure, the atomic species from the source arrive at the substrate without collision, but at higher pressure, they are thermalized by collision with the gas atoms in the chamber. At room temperature, $\lambda = 6/P$, where λ is the mean free path of the atom in millimeters and P is the pressure in pascals. Oxide thin films are used as tunnel barriers, and as functional elements in thin film stacks (ferromagnetic, antiferromagnetic, ferroelectric oxides). The methods are now described in more detail. *In situ* measurement of the thicknesses of the thin films may be achieved using optical reflectometry or a quartz crystal monitor.

1.2.3.1 Physical Methods

Thermal Evaporation Resistive evaporation is a commonly-used vacuum deposition process in which electrical energy is used to heat a boat containing the charge or a filament that heats the material to be deposited up to the point of evaporation [27, 28]. The vapour condenses in the form of a thin film on the cold substrate surface. The method is restricted to materials with moderately low melting points to

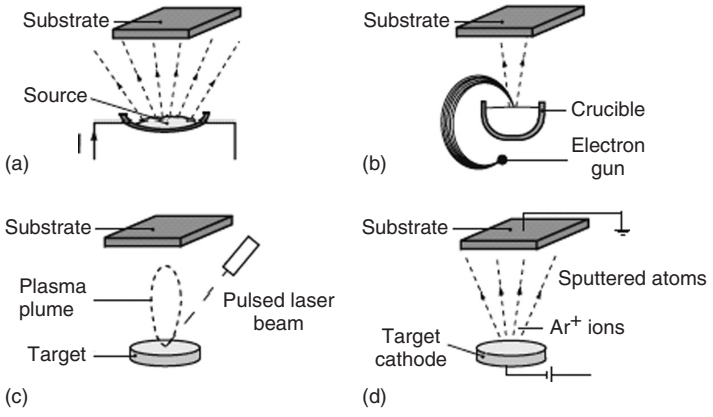

Figure 1.5 Methods for preparing thin films by a vapor or plasma condensing on a substrate: (a) thermal evaporation, (b) e-beam evaporation, (c) pulsed-laser deposition, and (d) sputtering.

avoid contamination by the boat, which is usually made of graphite, molybdenum, or tungsten.

E-Beam Evaporation Electron beam (e-beam) evaporation is a variant that is used, both for research and on an industrial scale, for making thin film coatings [28]. The technique involves bombarding a target of the material to be evaporated with a beam of high-energy electrons that may be swept over the surface of the target in a specific pattern with the help of beam focussing coils. The target is placed either directly in a water-cooled crucible or in a crucible liner that is made of a different material such as graphite or tungsten, which has a higher melting point than the target and does not form an alloy with it. As a result of the localized melting of the target, the material evaporates and is transported to a substrate. Another geometry utilizes a conducting target in the shape of a thin rod and the e-beam is electrostatically accelerated toward the end of the rod. As the material is evaporated, the rod is fed manually or automatically to keep a constant deposition rate. This geometry is used for materials with a very high melting point such as molybdenum or tungsten. E-beam evaporation can be used in a reactive environment to make thin films of oxides by evaporating a metallic target in the presence of reactive gas. In our case, the oxygen is either directly released into the evaporation chamber or introduced from a low-energy divergent-beam plasma ion source that is directed at the substrate. The latter technique, also known as ion-beam-assisted deposition (IBAD), produces more stoichiometric and better quality oxide films. Very high deposition rates can be achieved by e-beam evaporation compared to sputtering, which makes it advantageous for coating thick films. This technique is widely used to produce SiO_2, Al_2O_3, and some transition-metal oxides (TiO_2, HfO_2, and ZrO_2).

Molecular Beam Epitaxy (MBE) Molecular beam epitaxy (MBE) is a sophisticated version of vacuum evaporation [29]; it is a method of laying down layers of materials

a few atoms thick in ultrahigh vacuum (UHV). Molecular beams of the constituent elements are generated from heated sources and travel without scattering to a substrate where they combine to form an epitaxial film. The most common type of MBE source is the effusion cell (K-cell). The growth rate depends on the flux of material in the molecular beams, which can be controlled by the evaporation rate and, most importantly, switched on and off with shutters in a fraction of the time required to grow one monolayer. Typical growth rates are a monolayer per second or a micrometer per hour. MBE can produce high-quality layers with very abrupt interfaces and good control of thickness, doping, and composition. Because of the high degree of control, MBE is a valuable tool for development of sophisticated electronic and optoelectronic devices, but it is not used suited for industrial production.

Sputtering Sputtering is the preferred industrial thin film vacuum deposition technique, but it is also widely used in research laboratories. Sputtered films exhibit excellent, reproducibility, uniformity, density, purity and adhesion. It is possible to make oxides, nitrites, and other compounds of precise composition by reactive sputtering from metal targets [28, 30]. In *dc sputtering*, substrates are placed in the vacuum chamber, and it is evacuated to high vacuum before a low pressure (0.05–1 Pa) of the process gas, usually argon, is introduced. Sputtering starts when a negative potential of a few hundred volts is applied to the target material to be deposited, causing a plasma or glow discharge. Positively charged Ar^+ ions generated in the plasma collide with the negatively biased target. The momentum transfer ejects atomic-scale particles from the target, which traverse the chamber and are deposited as a thin film on the surface of the substrate. A magnetic field is usually created near the target surface by means of an arrangement of permanent magnets, known as a *magnetron*, in order to improve the ionization efficiency. Oxygen is mixed with the argon sputtering gas to produce oxides from metal targets. Alternatively, to make oxide or other insulating films directly, the radio-frequency method of *rf sputtering* is employed. Here the power supply commonly operates at 13.56 MHz. For part of the cycle, Ar ions bombard the target; for the rest of the cycle, electrons neutralize the build up of positive charge. Electrons also ionize the argon to create the plasma. Sputtering systems often have multiple targets, which permit the fabrication of complex thin film stacks used for spin electronic applications. An argon pressure of 0.02 Pa is usually sufficient to maintain a radio-frequency discharge.

Pulsed Laser Deposition (PLD) Pulsed laser deposition (PLD) is the most versatile physical method to deposit small high-quality metallic and insulating films in the laboratory; it has been intensively developed since 1987 when it was applied to grow high-temperature superconductors [31]. The technique employs high-power UV laser pulses (typically $\sim 10^8 \times \mathrm{W\,cm^{-2}}$) to ablate ionized material from the surface of a ceramic target in vacuum. This ablation event produces a transient, highly- luminous directional plasma plume that expands rapidly away from the target surface. The plume deposits material onto the substrate and a thin film is

formed. The plume is stoichiometrically similar to the target, and so thin films of roughly the same composition as of the target can be easily produced. Uniform thickness and composition can be achieved by rastering the laser spot across the target surface and/or moving the substrate during deposition. Targets often usually dense ceramic disks of 10–25 mm in diameter. The laser commonly used for oxide growth is a KrF excimer laser ($\lambda = 248$ nm), but frequency-doubled or tripled Nd-doped yttrium aluminum garnet (YAG) lasers are also used. The energy of the beam can range from 100 to 500 mJ per pulse, and typical fluences of 1– 5 J cm^{-2} are incident on the target. The repetition rate varies between 1 and 20 Hz. The vacuum chamber can be partially filled with oxygen or nitrogen to allow deposition at higher pressures.

A problem with the method is that liquid droplets or particulates may contaminate the plume and settle on the surface of the film. This can be avoided by off-axis deposition, where the substrate is parallel to the plume. Alternatively, the droplets may also be trapped by rapidly rotating mechanical filters, which feature in the PLD tools that are being developed for the industrial production of ferroelectric films.

1.2.3.2 Chemical Methods

Chemical Vapor Deposition (CVD) The growth of thin films by chemical vapor deposition (CVD) is an industrially significant process with good stability and reproducibility, which is used in a wide array of applications. CVD involves depositing a solid film from a gaseous molecular precursor [27]. Different energy sources, precursor gases, and substrates are used, depending on the desired product, but the precursors must be volatile, yet stable enough to be able to be delivered to the reactor where the volatilized precursor (such as silane, an organometallic, or a metal coordination complex) is passed over a heated substrate. Thermal decomposition of the precursor produces a thin film deposit, and ideally, the ligands associated with the precursor are cleanly lost to the gas phase as reaction products. Pressure and temperature are the important variables.

Chemical Vapor Transport The method, akin to that used to grow single crystals, entails the reversible conversion of nonvolatile elements and chemical compounds into volatile derivatives [25]. The volatile derivative migrates throughout a sealed reactor, typically a sealed, evacuated glass tube heated in a tube furnace. Because the tube is in a temperature gradient, the volatile derivative reverts to the parent solid, which is deposited as a thin film on the substrate and the transport agent is released at the opposite end of the tube to where it originated.

Atomic Layer Deposition (ALD) Atomic layer deposition (ALD) is based on sequential, self-limiting surface chemical reaction [32]. This unique growth technique can provide atomic layer control and allow ultrathin conformal films to be deposited on very high aspect ratio structures. ALD deposits films using pulses of gas that produce one atomic layer at a time. Within fairly wide process windows, the deposited film thickness is only dependent on the number of deposition cycles

providing extremely high uniformity and thickness control. ALD reactions are typically carried out in the range 200–400 °C. In particular, ALD is currently used in the semiconductor industry for high-k gate dielectrics (HfO_2, ZrO_2).

Dip Coating This is the main wet-chemical method to produce wide variety of oxide thin films such as ZnO, SnO_2, TiO_2, and $(Sn_{1-x}In_x)O_2$ (ITO). A substrate is dipped into a liquid coating solution of the chemical precursor and then gently withdrawn at a controlled rate. The thickness is determined by the balance of forces at the stagnation point on the liquid surface. A faster withdrawal rate pulls more fluid up onto the surface of the substrate before it has time to flow back into the solution. The thickness is also affected by fluid viscosity, density, and surface tension. Finally, the coating is cured by a conventional thermal treatment, or else UV, or IR irradiation.

Spray Pyrolysis A water-based precursor solution is sprayed through a nozzle onto a substrate where the atomized solution is dried and the metal oxide film is formed. It provides an easy way to dope any element in a required ratio through the solution medium. This method is convenient for preparing pinhole-free, homogenous, smooth thin films of oxides such as TiO_2 with controllable thickness. Spray pyrolysis can also be used to produce oxide powders.

1.3 Magnetic Properties of 3d and 4f Ions

One of the stranger truths of Nature is that magnetism is intimately associated with angular momentum. It is the angular momentum of charged particles, specifically that of the electrons that is responsible for the magnetism of solids. In the Bohr model, the z-component of orbital angular momentum $\boldsymbol{l}$ is quantized in units of $\hbar$. Regarding the Bohr atom as a loop of quantized current $I = -\mathrm{e}l/2\pi r^2 m_\mathrm{e}$, the magnetic moment $\boldsymbol{m} = I\mathcal{A} = -(\mathrm{e}\boldsymbol{l}/2\pi r^2 m_\mathrm{e})\pi r^2 = -(\mathrm{e}/2m_\mathrm{e})\boldsymbol{l}$. Here, $-\mathrm{e}$ and m_e are the charge and mass of the electron; the magnetic moment and angular momentum are oppositely aligned because of the electron's negative charge. The proportionality factor between magnetic moment and angular momentum, here $-(\mathrm{e}/2m_\mathrm{e})$, is known as the *gyromagnetic ratio*. However, angular momentum is quantized, with eigenvalues for the z-component being equal to $m_l\hbar$ where $m_l = 0$, ±1, ±2, $\ldots$ $\pm l$, so the orbital magnetic moment is also quantized, in units of the Bohr magneton

$$\mu_\mathrm{B} = \frac{e\hbar}{2m_\mathrm{e}}. \tag{1.1}$$

This quantity, equal to $9.27 \times 10^{-24}\,\mathrm{A\,m^2}$, is the fundamental unit of atomic-scale magnetism.

Besides angular momentum of orbital origin, the electron also possesses an intrinsic angular momentum $\boldsymbol{s}$ known as *spin*, a property common to all fermions. The corresponding gyromagnetic ratio for the electron is $-(e/m_\mathrm{e})$, so that $\boldsymbol{m} = -(e/m_\mathrm{e})\boldsymbol{s}$.

The two possible values for the spin moment of the electron are $m_z = -2\, m_s \mu_B = \mp 1\ \mu_B$ where $m_s = \pm 1/2$. The two spin states are often represented by arrows ↑ and ↓ and the *g-factor*, defined as the ratio of the magnitude of the magnetic moment in units of Bohr magneton to the magnitude of the angular momentum, in units of $\hbar$, is precisely 1 for orbital moments and practically equal to 2 for spin moments. The Zeeman Hamiltonian for the electron in a magnetic field **B** is therefore represented by the Hamiltonian

$$\mathcal{H}_Z = -\boldsymbol{m}\cdot\mathbf{B} = (\frac{\mu_B}{\hbar})(\boldsymbol{l}_z + 2\boldsymbol{s}_z)B \tag{1.2}$$

From the electron's point of view, it sees the nucleus orbiting around it, creating a magnetic field proportional to m_l, which interacts with the electronic spin moment. The celebrated spin–orbit interaction that is responsible for much that is important and useful in magnetism is represented by the Hamiltonian

$$\mathcal{H}_{so} = -\lambda \boldsymbol{l}\cdot\boldsymbol{s} \tag{1.3}$$

On passing from a single electron to a multielectron ion, the angular momentum of any filled (1s, 2s, 2p, etc.) shell is zero because both the spin moments and the orbital moments cancel each other. The moments residing in a partially filled 3d, 4d, 4f shell can be inferred from Hund's rules, namely: (i) maximize $S = \Sigma_i m_{si}$ for the i electrons in the shell, remembering that the orbitals can only accommodate one ↓ and one ↑ electron each, (ii) then maximize $L = \Sigma_i m_{li}$ consistent with S, and (iii) finally couple L and S to form the total angular momentum J so that $J = L - S$ if the shell is less than half full and $J = L + S$ if the cell is more than half full. When it is exactly half full, $\Sigma_i m_{li} = 0$; so $J = S$.

The magnetic moment of the free ion can be written as $g\mu_B J$, where the g-factor

$$g = \frac{3}{2} + \frac{[S(S+1) - L(L+1)]}{2J(J+1)} \tag{1.4}$$

Two examples:

1) Fe^{2+} ($3d^6$) has a spin occupancy of the 3d orbitals ↑↓ ↑ ↑ ↑ ↑ giving $S = 2$. The orbital sum is $L = 2$, hence $J = L + S = 4$ and $g = 3/2$.
2) Nd^{3+} ($4f^3$) has orbital occupancy of the 4f orbitals ↑ ↑ ↑ □ □ □ □ giving $S = 3/2$, $L = 6$ and $J = L - S = 9/2$ and $g = 4/3$.

The ground state of an ion is denoted by the term $^{2S+1}X_J$, where $2S+1$ is the spin degeneracy, and X = S, P, D, F, ... denotes the value of $L = 0, 1, 2, 3, \ldots$. The terms for free Fe^{2+} and Nd^{3+} ions are $^5D_4$ and $^4I_{9/2}$, respectively. The moment is now represented as $\boldsymbol{m} = -(\mu_B/\hbar)(\mathbf{L} + 2\mathbf{S})$. The Zeeman and spin-orbit interactions are represented respectively by the Hamiltonians

$$\mathcal{H}_Z = -\boldsymbol{m}\cdot\mathbf{B} = (\frac{\mu_B}{\hbar})(\mathbf{L}_z + 2\mathbf{S}_z)B \tag{1.5}$$

and

$$\mathcal{H}_{so} = -\Lambda \boldsymbol{L}\cdot\boldsymbol{S} \tag{1.6}$$

The above discussion concerned only the magnetism of free atoms or ions. About two-thirds of the atoms in the periodic table, and their isoelectronic free ions, have unpaired electrons and a net magnetic moment. However, when the ions are placed in the crystalline environment of a solid oxide, there are some drastic changes due to the influence of the oxygen neighbors. This is the *crystal-field* or *ligand-field interaction*. For 3d and 4d ions, it is stronger than the spin–orbit interaction, whereas for the 4f ions, which are well shielded from the outside world by the large filled 5s and 5p shells, the crystal field is screened so that it is only a perturbation on $\mathcal{H}_0 + \mathcal{H}_{so}$. (Table 1.4). For the rare earths, J is therefore a good quantum number, and the main effect of $\mathcal{H}_{cf}$ is to introduce single-ion anisotropy, whereby the ion may have one or more easy axes of magnetization in the crystal lattice.

For the 3d ions, the outer shell is unshielded from the environment, and the crystal-field interaction is stronger than the spin–orbit coupling. As a result, J is not a good quantum number. Orbital motion is impeded and the orbital moment is quenched. S is the good quantum number. From a magnetic viewpoint, the 3d ions in solids may be regarded as spin-only ions, with $m = g\mu_B S$ and $g \approx 2$. This is a welcome simplification, and it is supported by measurements of the paramagnetic susceptibility of crystals with dilute paramagnetic ions. The molar susceptibility of the ions is given by the Curie law $\chi_{mol} = C_{mol}/T$

$$\chi_{mol} = \mu_0 N_0 {p_{eff}}^2 {\mu_B}^2 / 3kT \tag{1.7}$$

where N_0 is Avogadro's number. In numerical terms,

$$C_{mol} = 1.571 \times 10^{-6} {p_{eff}}^2 \tag{1.8}$$

The effective Bohr magnetron number p_{eff} agrees with $g\sqrt{[J(J+1)]}$ for 4f ions, but for 3d ions, it is closer to $2\sqrt{[S(S+1)]}$. Some discrepancies appear, especially for Co^{2+}, where spin–orbit coupling restores a significant orbital contribution to the moment, and Eu^{3+}, which has a $J = 0$ ground state, but a low-lying $J = 1$ excited multiplet.

We focus first on the 3d ions, in order to explain how the crystal field influences both the electronic structure and magnetic properties of oxides. We begin with the *one-electron model* [33, 34], which ignores the onsite 3d–3d Coulomb interactions. This is a good approximation for d^1, d^4, d^6, and d^9 ions when Hund's first rule applies, as these ions have a single electron or hole outside an empty, a half-filled, or a filled shell.

When the ion is found in an undistorted tetrahedral or octahedral site in an oxide, the local environment has *cubic* symmetry unlike the *spherical* symmetry of

Table 1.4 Relative magnitudes of energy terms for 3d and 4f ions.

	$\mathcal{H}_0$	$\mathcal{H}_{so}$	$\mathcal{H}_{cf}$	$\mathcal{H}_Z$ in 1 T
3d	$1–5 \times 10^4$	$10^2–10^3$	10^4	1
4f	$1–6 \times 10^5$	$1–5 \times 10^3$	$\approx 3 \times 10^2$	1

a free ion. The free ion eigenfunctions ψ_0, $\psi_{\pm1}$, and $\psi_{\pm2}$, where the subscripts denote m_l, must be replaced by suitable linear combinations, which reflect the cubic symmetry. They are

$$\begin{aligned}
\psi_{xy} &= \left(\frac{-i}{\sqrt{2}}\right)(\psi_2 - \psi_{-2}) \\
\psi_{yz} &= \left(\frac{i}{\sqrt{2}}\right)(\psi_1 + \psi_{-1}) \\
\psi_{zx} &= \left(\frac{-1}{\sqrt{2}}\right)(\psi_1 - \psi_{-1}) \\
\psi_{x^2-y^2} &= \left(\frac{1}{\sqrt{2}}\right)(\psi_2 + \psi_{-2}) \\
\psi_{z^2} &= \psi_0
\end{aligned} \tag{1.9}$$

This basis set of d orbitals is illustrated in Figure 1.6.

We consider the influence of a crystal field due to an octahedron or tetrahedron of oxygen neighbors on the 3d wave functions. Considering the disposition of the oxygen orbitals in the octahedron, it is obvious that the *xy*, *yz*, and *zx* orbitals are degenerate – they are labeled as t_{2g} orbitals. It is less obvious that the $x^2 - y^2$ and z^2 orbitals, labeled as e_g, are degenerate, but they are clearly higher in energy because the electron density is maximum near the negatively charged anions. The crystal-field splitting is illustrated in Figure 1.7.

In the tetrahedral site, the splitting is reversed. The *e* orbitals are lower and the *t* orbitals are higher (the "g" subscript is dropped when there is no center of symmetry). The splitting in cubic coordination is similar (Figure 1.7).

The splitting cannot be entirely explained in terms of the electrostatic potential due to oxygen anions; about half is attributable to the different overlap of the *t* and *e* orbitals with the lower-lying 2p oxygen orbitals which introduces, in an octahedral site for example, greater bonding–antibonding splitting for the 2p-e_g σ-bonds than the 2p-t_{2g} π-bonds. This is known as the *ligand-field effect*. The magnitude of Δ_{oct} is of order 1 eV (Figure 1.8).

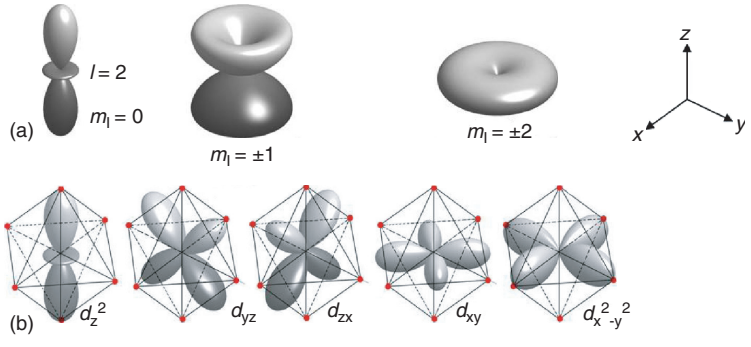

Figure 1.6 The 3d orbitals for a free ion (a) and the orbitals for the ion in a cubic crystal field (b).

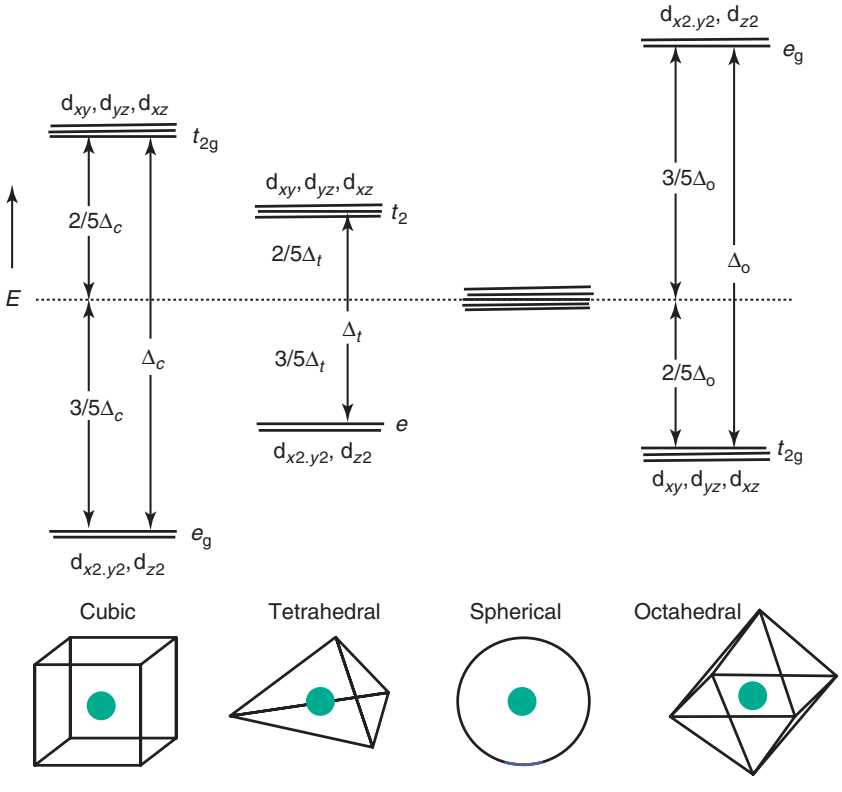

Figure 1.7 Crystal-field splitting for an ion in sites with octahedral, tetrahedral, and cubic coordination.

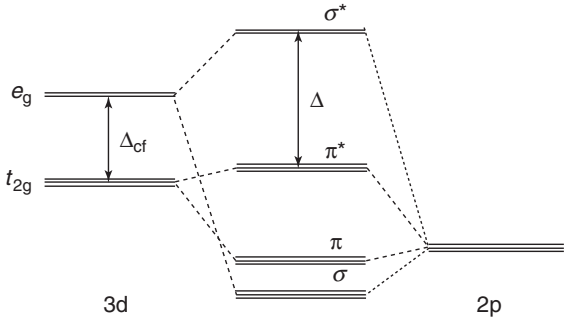

Figure 1.8 Illustration of the splitting of the t_{2g} and e_g orbitals in an octahedral environment. Δ_{cf} is the crystal-field splitting calculated in a point charge model. The extra ligand-field splitting due to the hybridization of 3d and sp orbitals gives the total splitting Δ.

The influence of a distortion, trigonal, tetragonal, or monoclinic, is to raise the degeneracy of the one-electron energy levels, as shown in Figure 1.9 for tetragonal distortion. The splitting preserves the center of gravity of the sets of orbitals.

The crystal-field stabilization energy, which contributes to the site preference of ions in crystal structures such as spinel where they have a choice, is calculated relative to the unsplit level. For example, for Cr^{3+} ($3d^3$) in octahedral sites, it is $3 \times (2/5)\Delta_{oct} = 1.2\ \Delta_{oct}$ whereas for Fe^{3+} ($3d^5$), it is zero. The cation radius and the 2p–3d mixing also influence site preference.

The *Jahn–Teller effect* is the tendency of some ions to spontaneously deform their local environment in order to improve their crystal-field stabilization energy. A $3d^3$ ion on an octahedral site gains nothing from a distortion of the oxygen octahedron, because of the center of gravity rule, but a $3d^4$ ion will tend to induce a tetragonal deformation that splits the e_g levels, lowering the energy of the occupied orbital, and hence of the ion (Figure 1.9). The Jahn–Teller effect is strong for d^4 and d^9 ions in octahedral coordination (Mn^{2+}, Cu^{2+}) and for d^1 and d^6 ions in tetrahedral coordination (V^{4+}, Co^{3+}). If the local strain is ε, the energy change $\Delta E = -A\varepsilon + B\varepsilon^2$, where the first term is the crystal-field stabilization energy D_{cfse} and the second term is the increased elactic energy. The J-T distorsion may be static or dynamic.

In the one-electron picture, the energy of an ion is obtained by populating the lowest orbitals with the available electrons. Hund's first rule implies that the five ↓ orbitals lie above the five ↑ orbitals by an amount $\mathcal{J}_H$, the on-site exchange energy

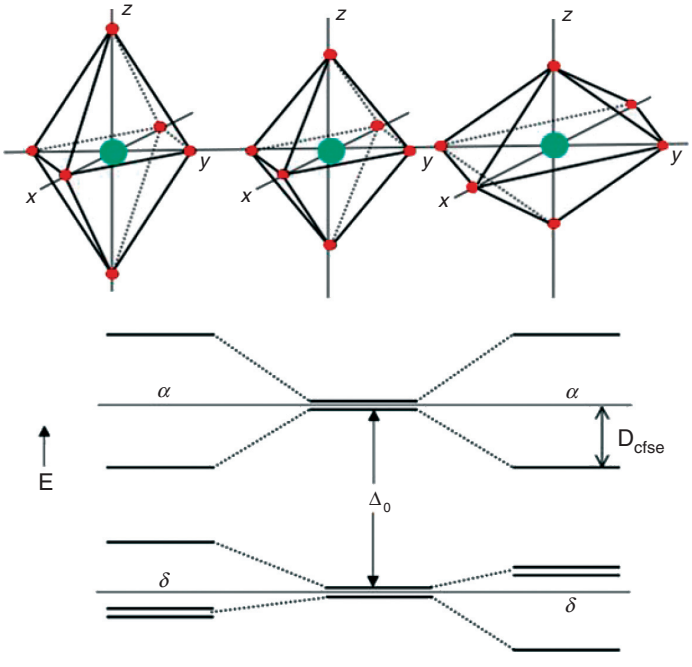

Figure 1.9 Influence of a tetragonal elongation or flattening of an octahedral site on the one-electron energy levels.

which is ≈1.5 eV. In some cases, however, $\Delta_{oct} > \mathcal{J}_H$, which means that the t_{2g} orbitals are filled before the e_g orbitals. This produces an ion in a *low-spin* state where Hund's rules no longer apply. In oxides, low-spin states are most frequently found for Co^{2+}, which has $S = 2$ in the high-spin state and $S = 1/2$ in the low-spin state.

Although the one-electron picture is relatively easy to grasp and can be readily related to energy-band calculations, it does not do justice to the many-electron interactions in 3d ions, especially for high-spin ions with two, three, seven, or eight 3d electrons, which are in an F-state. Ions with five electrons are in an S state, while those with one, four, six, or nine electrons are in a D state. Here S, D, and F refer to the values of L (0, 2, or 3) given by Hund's second rule. The excited states of the $3d^n$ shell that are probed in optical transitions have been calculated from crystal-field theory, and they are represented on Tanabe–Sugano diagrams [14].

Two interesting electronic effects that may be observed for 3d electrons in oxides are *charge order* and *orbital order* [35]. The first arises when a particular lattice site is occupied by an ion in a mixture of two different valence states. Examples are Mn^{4+} and Mn^{3+} or Fe^{3+} and Fe^{2+}. The average 3d occupancy is nonintegral, for example, 3.5 or 5.5, and it is possible for the extra 3d electron to hop rapidly among the d^3 or d^5 ion cores at a high enough temperature, or else it may settle on alternate sites with some lattice distortion in a charge-ordered state.

Orbital order arises when the 3d occupancy is integral, but in the undistorted, high-temperature phase, the electron occupies a degenerate orbital. An example is Mn^{3+} ($t_{2g}{}^3 e_g{}^1$). A lattice distortion such as tetragonal compression and expansion on alternate sites can lead to alternate occupancy of d_{z2} and d_{x2-y2} orbitals. The ordered states generally revert to disordered states at a high-temperature phase transition, where an entropy of approximately $R\ln 2$ is released, comparable to the entropy $R\ln(2S+1)$ released in the vicinity of a magnetic disordering transition. These ordering effects are discussed further in Section 1.4.

Crystal-field effects on the rare-earth ions in oxides are related to the energy levels of the highly correlated $4f^n$ shell, rather than to those of the individual 4f orbitals. The crystal-field Hamiltonian is often written as $\mathcal{H}_{cf} = \Sigma_{n,m} B_n{}^m \hat{\mathbf{O}}_n{}^m$, where $n = 0$, 2, 4, or 6 and $m \leq n$; $\hat{\mathbf{O}}_n{}^m$ are Stevens operators that are combinations of the angular momentum operators $\hat{\mathbf{J}}_i$ and $\hat{\mathbf{J}}^2$. The number and type of terms in the expansion depend on the site symmetry. Crystal-field parameters $B_n{}^m$ reflect both features of the 4f ion and features of the lattice site. These are separated in the more explicit formulation

$$\mathcal{H}_{cf} = \sum_{n,m} A_n{}^m \theta_n < r^n > \hat{\mathbf{O}}_n{}^m \tag{1.10}$$

where the crystal-field coefficients $A_n{}^m$ parameterize the derivatives of the electrostatic potential due to the lattice at the rare-earth site, $<r^n>$ is the average over the 4f electron distribution and θ_n is the 2^n-pole moment of the ion – quadrupole for $n = 2$, hexadecapole for $n = 4$ and 64-pole for $n = 6$. The expressions for uniaxial and cubic symmetry are, respectively,

$$\mathcal{H}_{cf} = B_2{}^0 \hat{\mathbf{O}}_2{}^0 \tag{1.11}$$

and

$$\mathcal{H}_{cf} = B_4{}^0\hat{\mathbf{O}}_4{}^0 + 5B_4{}^4\hat{\mathbf{O}}_4{}^4 \tag{1.12}$$

where the Stevens operators are

$$\hat{\mathbf{O}}_2{}^0 = 3\hat{\mathbf{J}}_z{}^2 - J(J+1)$$

$$\hat{\mathbf{O}}_4{}^0 = [35\hat{\mathbf{J}}_z{}^4 - 30J(J+1)\hat{\mathbf{J}}_z{}^2 + 25\hat{\mathbf{J}}_z{}^2 - 6\,J(J+1) + 3J(J+1)^3]$$

and

$$\hat{\mathbf{O}}_2{}^4 = \tfrac{1}{2}[\hat{\mathbf{J}}_+{}^4 + \hat{\mathbf{J}}_-{}^4]$$

[36, 37]. The charge densities for the $4f^n$ ions are shown (with exaggerated asphericities) in Figure 1.10. The quadrupole moments θ_2 reflect the oblate or prolate shape of the charge distribution and follow the quarter-shell rule; they are negative for Ce, Pr, Nd, Tb, Dy, and Ho but positive for Sm, Er, Tm, and Yb. (Trivalent Eu has $J = 0$, and Pm is unstable; so it is not shown.)

The same formalism may be applied for the 3d ions, but the averages are over the 3d shell and the Stevens operators now involve **L** rather than **J** and only run up to $n,m = 4$ [37]. The uniaxial anisotropy energy can be represented by a term

$$\mathcal{H}_a = D\hat{\mathbf{J}}_z{}^2 \tag{1.13}$$

for the rare earths, and a spin Hamiltonian

$$\mathcal{H}_a = D\hat{\mathbf{S}}_z{}^2 \tag{1.14}$$

for the 3d ions. For non-S-state 3d ions in noncubic sites, D/k may be of the order of one Kelvin (0.1 meV). Single-ion magnetic anisotropy, expressed as an energy per ion, is a weak interaction. It determines the directon of sublattice magnetization in oxides.

1.4 Magnetic Interactions in Oxides

Exchange interactions are symmetry-constrained coulomb interactions that have the effect of coupling electronic spins. Intraionic exchange, also known as $\mathcal{J}_H$ or

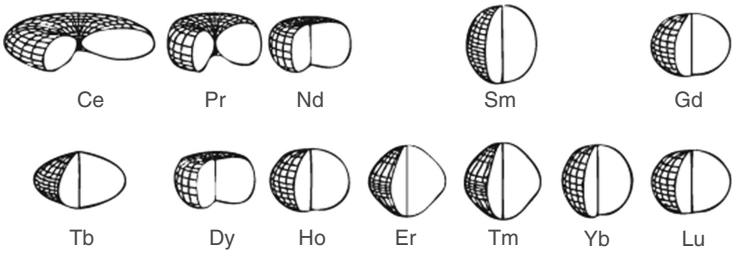

Figure 1.10 The charge densities for the trivalent rare-earth ions.

Hund's rule exchange, couples electrons in a partially filled shell on an ion so as to maximize the total spin (Hund's first rule). In oxides, it is normally greater than the crystal/ligand-field splitting Δ so that the $\uparrow$ orbitals are filled first, before beginning to fill the $\downarrow$ orbitals. If $\Delta > \mathcal{J}_H$, the ion enters a low-spin state, in conflict with Hund's first rule. The rules were formulated for free atoms and ions. The magnitude of $\mathcal{J}_H$ in the 3d series is about 1.0-2.0eV.

Interionic exchange, coupling the spins on adjacent ions, is much weaker. It depends on the overlap of exponentially decaying wave functions, and does not usually exceed 0.01 eV. However, it is responsible for the magnetic order of the ionic spins already created by the intraionic coupling. Interionic exchange between a pair of ions i, j is described by the Heisenberg Hamiltonian

$$\mathcal{H}_{ex} = -2\mathcal{J}_{ij}\mathbf{S}_i \cdot \mathbf{S}_j \tag{1.15}$$

Heisenberg exchange $\mathcal{J}$ may couple the pair of spins parallel or antiparallel, depending on its sign. The interaction is summed over all pairs of ions, but in oxides, the sum is largely restricted to a few nearest-neighbor shells. The exchange parameters $\mathcal{J}_{ij}$ determine the magnetic ordering temperature and the spin-wave dispersion relations. An important difference between ferromagnetic ($\mathcal{J} > 0$) and antiferromagnetic ($\mathcal{J} < 0$) interactions is that the latter are subject to geometric frustration owing to lattice topology [11].

1.4.1 Superexchange

Antiferromagnetic exchange interactions are responsible for the antiferromagnetic order in oxides such as NiO, $CaMnO_3$, or Fe_2O_3. There is little direct overlap of the wave functions of the nearest-neighbor cations, but they overlap strongly with the 2p orbitals of the neighboring O^{2-} anions. The oxygen bridges transmit a *superexchange* interaction via the hybridization between 2p orbitals and 3d orbitals. The interaction involves two virtual electron transfers. First an electron is transferred from the oxygen $2p^6$ shell to an adjacent M_1 ion, leading to a virtual d^{n+1} state, at an energy cost U. Then the 2p hole is then filled by electron transfer from another M_2 ion, which overlaps with the same 2p shell. This has the effect of coupling the spins of M_1 and M_2. A simple case is shown in Figure 1.11,where M_1 and M_2 are ions with a half-filled d shell (Fe^{3+}, Mn^{2+}), which overlap with the same 2p orbital. Then transfer of a p $\downarrow$ electron into an empty 3d $\downarrow$ state of M_1 (the 3d $\uparrow$ states are all full) leaves a 2p $\downarrow$ hole, which can only be filled by a 3d $\downarrow$ electron from M_2. Hence the configuration in Figure 1.11(b) is lower in energy than the configuration in Figure 1.11(a). Both electrons in the oxygen 2p orbital can then spread out into unoccupied 3d orbitals when the ion spins are antiparallel; the superexchange interaction $\mathcal{J}$ is therefore negative [38]. Since superexchange interactions involve simultaneous virtual transfer of two electrons with the instantaneous formation of a $3d^{n+1}2p^5$ excited state, the interaction is of order $-2t^2/U$, where t is the p–d transfer integral and U is the on-site 3d Coulomb interaction. The transfer integral is of the order of 0.1 eV, and the on-site Coulomb interaction is 2 eV or more so the interaction

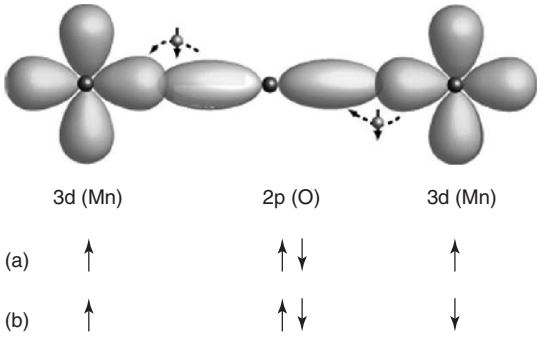

Figure 1.11 A typical superexchange bond. Antiferromagnetic configuration (b) is lower in energy than ferromagnetic configuration (a).

is of order 0.01 eV (∼100K). $\mathcal{J}$ depends sensitively on the interatomic separation, and also on the M–O–M bond angle, θ_{12}, varying as $\cos^2\theta_{12}$.

The occupancy and orbital degeneracy of the 3d states is the critical factor in determining the strength and sign of superexchange. There are many possible cases to consider and they were discussed by Goodenough in his book [6]. The results were summarized in the Goodenough–Kanamori rules, which were reformulated by Anderson, in a simpler way that makes it unnecessary to consider the oxygen.

1) When two cations have lobes of singly occupied 3d orbitals that point toward each other, giving large overlap and hopping integrals, the exchange is strong and antiferromagnetic ($\mathcal{J} < 0$). This is the usual case, for 120°–180° M–O–M bonds.
2) When two cations have an overlap integral between singly occupied 3d orbitals which is zero by symmetry, the exchange is ferromagnetic and relatively weak. This is the case for ∼90° M–O–M bonds.
3) When two cations have an overlap between singly occupied 3d orbitals and empty or doubly occupied orbitals of the same type, the exchange is also ferromagnetic, and relatively weak.

Superexchange is more commonly antiferromagnetic than ferromagnetic, because the overlap integrals are likely to be larger than zero.

1.4.2 Double Exchange

This interaction arises between 3d ions that have both localized and delocalized electrons [39]. Unlike ferromagnetic superexchange, a mixed-valence configuration is required for double exchange. In a mixed-valence manganite such as $(La_{1-x}A_x)MnO_3$, A = Ba, Ca, Sr, the two Mn valence states are imposed by the charge states of the other ions in the compound, La^{3+}, A^{2+}, and O^{2-}. The d^3 core electrons for the octahedrally coordinated Mn ions are localized in a narrow $t_{2g}\uparrow$ band, but the fourth d electron inhabits a broader $e_g\uparrow$ band, hybridized with

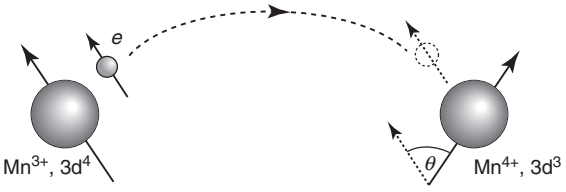

Figure 1.12 The double exchange interaction. The fourth delocalized electron in Mn^{3+} ion hops to its neighboring Mn^{4+} without changing its spin.

oxygen, where it can hop from one d^3 core to another, as shown in Figure 1.12. The configurations ${d^3}_i{d^4}_j$ and ${d^4}_i{d^3}_j$ on adjacent sites i and j are practically degenerate. On each site, there is a strong on-site Hund's rule exchange coupling $\mathcal{J}_H \approx 2\,eV$ between t_{2g} and e_g electrons, which is very much greater than the hopping energy. Electrons can hop freely if the core spins are parallel, as the delocalized electron does not have to change its spin direction, but when they are antiparallel, there is a large energy barrier due to the Hund's rule interaction. The ability to hop increases the extent of the d wavefunction and reduces the kinetic energy. Hence, the overall energy saving leads to ferromagnetic alignment of the spins of neighboring ions.

If the quantization axes of adjacent sites are misaligned by an angle θ, the eigenvector of an electron in the rotated frame is $(\cos\theta/2, \sin\theta/2)$. The transfer integral t therefore varies as $\cos(\theta/2)$. Double exchange is ferromagnetic because the transfer is zero when the ions on adjacent sites are antiparallel, $\theta = \pi$.

Another common double-exchange pair is Fe^{3+} and Fe^{2+}, which are d^5 and d^6 ions, respectively. The d^5 configuration is a half-filled, $\uparrow$ d shell, and the sixth, $\downarrow$ d electron occupies the bottom of a $t_{2g}\uparrow$ band when the ion is octahedrally coordinated by oxygen, where it can hop directly from one d^5 $\uparrow$ core to another.

The effective Hamiltonian of double exchange also has the characteristic scalar product $(\mathbf{S}_i \cdot \mathbf{S}_j)$; however, it contains not only this term but also higher powers of it. The highest power is determined by the magnitude of the localized spins:

$$\mathcal{H}_{DE} \sim \sum_{n=0}^{2s} J_n(S)(\mathbf{S}_i \cdot \mathbf{S}_j)^n \tag{1.16}$$

When $\mathcal{J}_n(S)$ for $n \geq 2$ is not negligible, then $\mathcal{H}_{DE}$ is not of Heisenberg type [40]. However, the bilinear term, which always dominates, is always ferromagnetic.

Double exchange differs clearly from superexchange in the following respect: in superexchange, the electrons do not actually move between the two metal cations – the occupancy of the d shell of the two metal ions remains the same. In double exchange, the electrons are itinerant; they hop between the positive ions via the intermediate ligand (oxygen); this results in the material displaying from electrical conductivity as well as magnetic exchange coupling.

1.4.3 Antisymmetric Exchange

In crystals with uniaxial or lower symmetry, a weak interaction of the form

$$\mathcal{H}_{\mathrm{Dm}} = -\boldsymbol{\mathcal{D}} \times (\mathbf{S}_i \times \mathbf{S}_j) \tag{1.17}$$

was proposed by Dzyaloshinskii and Moriya. The vector $\boldsymbol{\mathcal{D}}$ lies along the axis of symmetry, but its magnitude is only about 1% of $\mathcal{J}$. The effect of the interaction is to cant the spins away from the antiferromagnetic axis, producing a weak intrinsic ferromagnetic moment in a direction perpendicular to the antiferromagnetic axis. The most famous example is hematite, αFe_2O_3.

1.4.4 Direct Exchange

Direct exchange is dominant in metals but relatively unimportant in oxides. Two examples where it is operative are the d-band metals CrO_2 and $SrRuO_3$. Direct electron hopping in the partly filled t_{2g} band of Cr in the rutile structure is a ferromagnetic interaction; two of the three t_{2g} orbitals that form the π^* band (Figure 1.8) are filled, and the other is empty [41].

1.4.5 Orbital Order

We mentioned in Section 1.3 that interionic electrostatic interactions can also give rise to orbital order [42]. When there is a single occupied d orbital at each 3d ion site, antiparallel spin alignment on adjacent sites favors electron hopping and thus reduces the energy of the system (antiferromagnetic superexchange). However, if two degenerate orbital states are available, it is possible for the electron spins to hop to their neighbors with parallel spins, filling the other orbital, which may also lower the energy. In this case, spin order (ferromagnetism) is possible on the condition that different degenerate neighboring 3d orbitals are occupied in an alternating array (Figure 1.13a). By analogy with spin order, two possible choices of orbital can be described by a pseudospin T. Consider, for example, a $3d^4$ ion with one electron in the degenerate $d_{x^2-y^2}$ and d_{z^2} states in an octahedral site; when $d_{x^2-y^2}$ is occupied, the orbital order parameter is $T_z = 1/2$ and when d_{z^2} is occupied, it is $T_z = -1/2$ [43]. The pseudospin interaction $-2\mathcal{K}\, T_i \cdot T_j$ is antiferromagnetic and there is an interaction between the spin and pseudospin, of S and T, between different ions. This exchange interaction is represented by the following generalized Heisenberg Hamiltonian:

$$\mathcal{H} = -2\sum_{ij}[J_{ij}(T_i, T_j)S_iS_j + K_{ij}(T_i, T_j)] \tag{1.18}$$

The interactions $\mathcal{J}_{ij}$ and $\mathcal{K}_{ij}$ originate from the quantum mechanical process with intermediate virtual states (Figure 1.13).

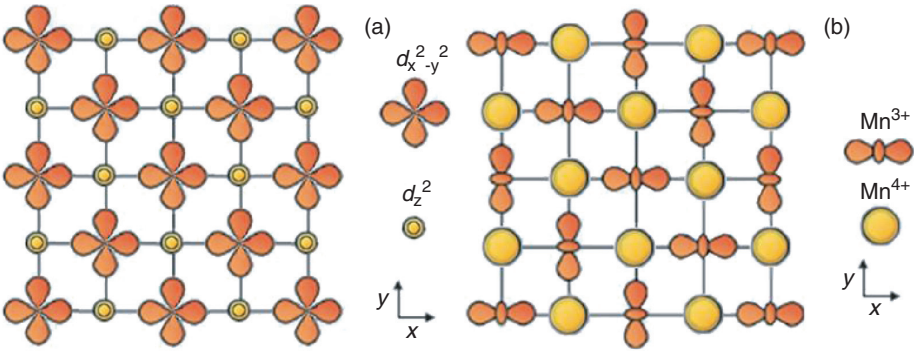

Figure 1.13 Examples showing orbital order of the x^2-y^2/z^2 type (a) and both orbital order of the $x^2/y^2/z^2$ type and charge order projected onto an MnO_2 plane (b).

In more general cases, the transfer integral t_{ij} depends on the direction of the bond ij relative to the pair of orbitals $d_{x^2-y^2}$ or d_{z^2}. This gives rise to anisotropy of the Hamiltonian in pseudospin space as well as in real space. In many respects, analogies can be drawn between S and T, in spite of the anisotropy in T space. However, one aspect that is special to T is Jahn–Teller coupling. When the two apical O atoms move toward the ion, the energy of d_{z^2} becomes higher than $d_{x^2-y^2}$, and the degeneracy is lifted. The Jahn–Teller effect is represented by the following Hamiltonian for a single octahedron:

$$\mathcal{H}_{\mathrm{JT}} = -g(T_x Q_2 + T_z Q_3) \tag{1.19}$$

where (Q_2, Q_3) are the coordinates for the displacements of O atoms surrounding the transition-metal atom and g is the elastic coupling constant. Whenever long-range orbital order exists, $<T_x> 0$ and $<T_z> 0$, the Jahn–Teller distortion is always present.

1.4.6 Charge Order

In a mixed-valence oxide, the repulsive coulomb interactions among the extra, mobile electrons will force them apart. If the site occupancy is a rational fraction such as $1/2$, there is a possibility that they will adopt a nonconducting, regular charge-ordered arrangement—a phenomenon known as *Wigner crystallization*. Charge ordering occurs in $La_{1-x}Ca_xMnO_3$ with $x = 0.5$, below the critical temperature $T_c = 160$ K; where a charge-ordered antiferromagnetic state has been found.

The original example of a charge-ordering transition was magnetite, Fe_3O_4. Verwey proposed in 1939 that the electrons belonging to Fe^{2+} in B-sites of the spinel lattice undergo a charge-ordering transition below 120 K, forming a superlattice, which is now known as the *Verwey transition*. In fact, charge ordering is never this simple. The ionic charge states are not integral; they are close to

$n \pm \varepsilon$, where ε is of the order of 0.1. Recently, the charge-ordered structure has been solved using diffraction of synchrotron radiation on a small, untwined crystal of magnetite [44]. The complex, charge-ordered structure is represented by the superposition of many different charge density waves.

1.5 Concentrated Magnetic Oxides

Oxides exhibit a wide range of electric, magnetic, optical, and structural properties [9, 10, 11]. They can be insulating, semiconducting, metallic, ferroelectric, piezoelectric, ferromagnetic, ferrimagnetic, antiferromagnetic, or superconducting. A short account of each of the most common magnetic oxides is given in this section, and some related compounds are mentioned. Properties are summarized in Table 1.5. The dominant magnetic coupling in transition-metal oxides is normally antiferromagnetic superexchange, leading to antiferromagnetic or ferrimagnetic order. Ferromagnetism is usually associated with mixed valence and double exchange.

1.5.1 αFe_2O_3

The most abundant magnetic oxide is αFe_2O_3 (hematite). It is an insulating, deep-red rock-forming mineral with the rhombohedral corundum (sapphire) structure. Strong antiferromagnetic superexchange between the $3d^5$ ferric cations mediated by the $2p^6$ O^{2-} anions leads to an exceptionally high Néel temperature, $T_N = 960$ K. The easy axis below $T_M = 265$ K is the rhombohedral 111 axis, which corresponds to the c-axis. of the hexagonal close-packed oxygen lattice. Above T_M, known as the *Morin transition* temperature, the balance of lattice dipole and magnetocrystalline anisotropy energies changes sign, and the moments lie in the basal plane [45, 46]. The in-plane moments are no longer strictly collinear, because of the weak Dzyaloshinskii–Moriya interaction, Eq. 1.17, where the interaction vector $\mathcal{D}$

Table 1.5 Structural and magnetic properties of magnetic oxides [11].

Material	Structure		Order	m_0 (μ_B fu^{-1})	$\mu_0 M_s$ (T)	T_C or T_N (K)	Transport
NiO	Cubic	$Fm\underline{3}m$	Af	—	—	525	Insulator
Fe_2O_3	Rhombohedral	$R\underline{3}c$	cAf	0.005	0.003	960	Insulator
Fe_3O_4	Cubic	$Fd3m$	Ferri	4.0	0.60	860	Half metal
$Y_3Fe_5O_{12}$	Cubic	$Ia3d$	Ferri	5.0	0.18	560	Insulator
$BaFe_{12}O_{19}$	Hexagonal	$P6_3/mmc$	Ferri	20.0	0.48	740	Insulator
CrO_2	Tetragonal	$P4_2/mnm$	Ferro	2.0	0.49	396	Half metal
$La_{0.7}Sr_{0.3}MnO_3$	Rhombohedral	$R\underline{3}m$	Ferro	3.6	0.55	360	Half metal
Sr_2FeMoO_6	Orthorhombic	$P4/mmm$	Ferri	3.6	0.25	425	Half metal
$Tl_2Mn_2O_7$	Cubic	$Fd\underline{3}m$	Ferro	4.2	0.40	118	Semimetal

(≈0.1 K) must lie along the *c*-axis for symmetry reasons. The average value of $\mathcal{J}$ is ≈20 K and the slight canting of the antiferromagnetic sublattices at an angle of order $\mathcal{D}/\mathcal{J}$ produces a weak resultant magnetization of 2.5 kA m^{-1}. Although Fe^{3+} is an S-state ion with no orbital moment and no magnetocrystalline anisotropy to first order, the off-diagonal crystal-field terms mix some of the orbital character of the excited states into the ground site, leading to magnetocrystalline anisotropy. The magnetic dipole field at the Fe sites is about 1 T (only in cubic lattices does it sum to zero), giving an energy expression Eq. (1.14) with $\mathcal{D} \approx 0.4$ K at room temperature. The two contributions have slightly different temperature dependences, varying as $<Sz^2>$ and $<Sz^2>$, which leads to the spin reorientation at the Morin transition when their sum changes sign [46].

Ti, V, Cr, and Mn also form sesquioxides with the corundum structure. Of these, the most interesting is Cr_2O_3, which has a different antiferromagnetic stacking below its Néel point $T_N = 306$ K. It exhibits no spin reorientation, but it is *magnetoelectric*. This means that a small magnetic moment can be induced by an electric field.

1.5.2
Fe_3O_4

Magnetite is the other common rock-forming iron oxide, and the most famous magnetic mineral. It is a black conductor, with the inverse spinel structure. The octahedral sites {} are occupied by an equiatomic mixture of ferric and ferrous iron with rapid Fe^{2+}–Fe^{3+} electron hopping, while the tetrahedral sites [] are exclusively occupied by ferric cations. The formula can be written as $[Fe^{3+}]\{Fe^{2}Fe^{3+}\}O_4$. The octahedral and tetrahedral sublattices are coupled antiparallell by superexchange, giving a ferrimagnetic structure with a net moment of about 4 μ_B and a room-temperature magnetization of 480 kA m^{-1}. The Curie temperature is 860 K. The mobile electron associated with Fe^{2+} ↓ on the octahedral sites occupies a 1/6-filled minority-spin t_{2g} band; the average B-site configuration is $3d^n$ $(t_{2g}{}^3 e_g{}^2)^{\uparrow}(t_{2g}{}^{0.5})^{\downarrow}$ with $<n> = 5.5$; so magnetite was expected to be a half metal with a spin gap in the majority density of states [47]. However, there is little evidence for an exceptionally high-spin polarization at room temperature. The 3d conduction electrons interact electrostatically with the oxygen anions to form small polarons with large effective mass, which move among the B-sites by thermally activated hopping [48].

Magnetite undergoes its celebrated Verwey transition at 120 K [44, 49]. This is an insulator–metal transition where the conductivity decreases abruptly by a factor of ~100 and the symmetry of the crystal is lowered from cubic to monoclinic. Verwey's original model of regular charge ordering of Fe^{3+} and Fe^{2+} ions on octahedral sites [49] was oversimplified, and a complex ordering of fractional charges on these sites with iron trimer motifs has now been established, which is described by the superposition of 128 atomic displacement waves [44].

There is an important family of insulating *spinel ferrites*, of which the main members are $ZnFe_2O_4$, $MgFe_2O_4$, $MnFe_2O_4$, $CoFe_2O$, $NiFe_2O_4$, and $Li_{0.5}Fe_{2.5}O_4$. Only the first of these has the normal cation distribution; the others are inverse

with Fe^{3+} on tetrahedral sites. Lithium ferrite has the highest Curie temperature of 943 K. Cobalt ferrite has by far the greatest cubic magnetocrystalline anisotropy and magnetostriction, with [100] easy axes, whereas all the others have [111] easy axes. Nickel–zinc ferrite and manganese–zinc ferrite are widely used as cores in high-frequency inductors.

γFe_2O_3 also has the spinel structure, with vacant octahedral sites; the formula may be written as $[Fe]\{Fe_{5/3}\square_{1/3}\}O_4$. The compound is a known insulator, with a moment of $3.3\,\mu_B$ per formula. The structure converts to αFe_2O_3 on heating above 800 K. Acicular Co:γFe_2O_3 powder is still produced for particulate magnetic recording media.

1.5.3
NiO

Nickel oxide has the cubic NaCl structure with a tiny rhombohedral distortion. It is an antiferromagnetic charge-transfer insulator [50] with a Néel temperature of 525 K [51]. The Ni^{2+} ions have a $3d^8$ configuration with $S = 1$. Moments are arranged in ferromagnetic (111) planes perpendicular to the 111 direction, with the spins in adjacent planes oriented antiferromagnetically [51]. Nonstoichiometric nickel oxide $Ni_{1-\delta}O$ exhibits p-type semiconducting properties owing to the presence of holes in the oxygen 2p band. Stoichiometric NiO was used for exchange bias of early spin-valve structure.

Other antiferromagnetic monoxides with the NaCl structure are MnO, FeO, and CoO. Their Néel temperatures are below room temperature. EuO is an interesting insulating ferromagnet, with $4f^7$, $S = 7/2$ ions and a Curie temperature of 69 K.

1.5.4
$Y_3Fe_5O_{12}$

Garnets are cubic oxides with a large unit cell and general formula $<A_3>[B_2]\{X_3\}O_{12}$, where the brackets, <>, [], and {} denote sites with eightfold (cubic), tetrahedral, and octahedral coordination [52]. Pyrope, $<Mg_3>[Al_2]Si_3\}O_{12}$, was a natural example. The magnetic garnets are ferrites with formula $R_3Fe_5O_{12}$, where the antiparallel octahedral and tetrahedral sublattices are filled with Fe^{3+} ions, yielding a net ferromagnetic moment of $5\,\mu_B$ per formula and a net magnetization of $140\,kA\,m^{-1}$ for the iron. R is a trivalent rare-earth ion – Y^{3+} in the case of YIG. This material is a green insulator with a Curie temperature of 560 K and little magnetocrystalline anisotropy. It is widely used for microwave components such as filters and circulators on account of its very narrow ferromagnetic resonance linewidth and excellent insulating properties. YIG is vital for modern radio-frequency communications.

Iron garnets form for the whole series of rare earths from Pr to Lu. The rare-earth sublattice is weakly coupled to iron in the sense that the moment of Gd and the other magnetic heavy rare earths couple antiparallel to the resultant iron moment of $5\,\mu_B$ per formula at low temperature. Because of the weak coupling, the rare-earth

magnetization falls off much more rapidly than that of the net iron magnetization with increasing temperature. As a consequence, there is a temperature, known as the *compensation temperature* T_{comp}, where the two exactly cancel. Its value for $Gd_3Fe_5O_{12}$ (GIG) for example is 285 K. A feature of the magnetism near the compensation temperature is that the coercivity grows as the magnetization disappears. Some data for GIG are shown in Figure 1.14. The explanation is that the coercivity, which depends on the defects and microstructure of the oxide, is usually a small fraction (<25%) of the anisotropy field H_a,

$$H_a = 2K/\mu_0 M_s \tag{1.20}$$

where K is the anisotropy constant and M_s is the net magnetization. As the magnetization falls to zero, the anisotropy field and the coercivity tend to diverge,

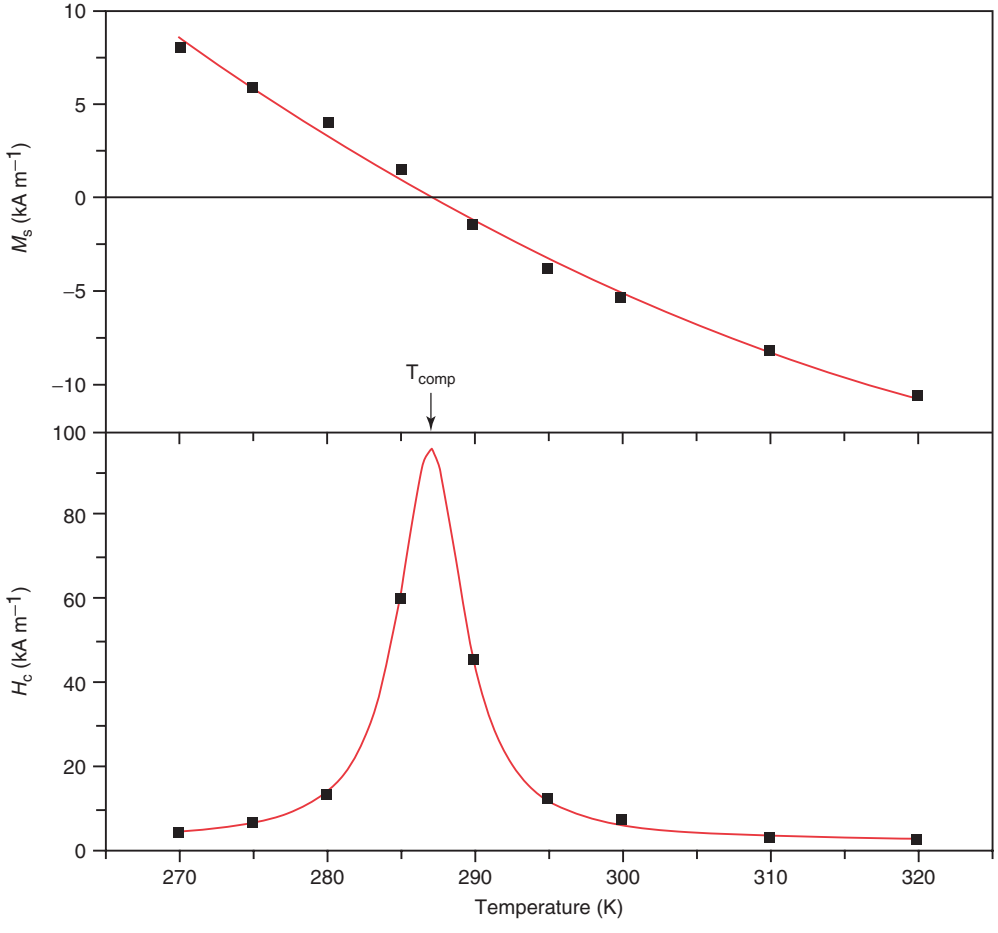

Figure 1.14 Magnetization and coercivity of $Gd_3Fe_5O_{12}$ powder in the vicinity of the compensation temperature at 285 K.

as seen in Figure 1.14b. Hematite, which has a very weak magnetization above T_M, exhibits substantial coercivity for a similar reason.

Garnets doped with Bi^{3+} ions exhibit a substantial magneto-optic Faraday effect on account of the large spin–orbit coupling associated with heavy atoms. Thin films were used for magnetooptic recording based on compensation-point writing where a spot of the film was heated well above T_{comp} and cooled in a field greater than the coercivity at the elevated temperature. At ambient temperature, which is close to T_{comp}, the increase in coercivity ensured the stability of the recorded bit [52]. The method is now obsolete, but heat-assisted magnetic recording is being developed to write on modern hard disc media which have very high coercivity at room temperature.

1.5.5
$SrFe_{12}O_{19}$

Strontium and barium ferrite crystallize in the hexagonal magnetoplumbite structure. The large hexagonal cell includes six cation sites, one for the large divalent alkaline earth and five for the ferric ions, three of them octahedral, one tetrahedral, and one trigonal bipyramidal site with fivefold oxygen coordination. The compound is ferrimagnetic, with a Curie temperature of 740 K [53]. In the unit cell, there are eight ferric ions on the majority sublattice and four on the minority sublattice, leading to a net moment of $20\,\mu_B$ per formula at $T = 0$ and a room-temperature magnetization of 380 kA m^{-1}. Even though all the magnetic ions are all ferric, there is sufficient anisotropy arising from the bipyramidal and distorted octahedral sites in the structure to produce uniaxial anisotropy of $K_1 = 300$ kJ m^{-3}, which ensures that the magnetic hardness parameter, defined as

$$\kappa = (K_1/\mu_0 M_s^{\,2})^{1/2} \tag{1.21}$$

is 1.35, sufficient to make a true permanent magnet. The hexagonal ferrites were the first low-cost materials that could be manufactured into magnets of any desired shape. Nowadays, around a million tonnes of these sintered and bonded ceramic magnets are produced annually.

1.5.6
$(La,Sr)MnO_3$

Many magnetic and superconducting oxides crystallize in the perovskite structure, or in its derivatives. The basic cubic cell with a lattice parameter $a_0 \approx 390$ pm contains just two cations: one is usually an alkaline earth or rare-earth cation, and the other a 3d cation. The mineral perovskite $CaTiO_3$ is uncommon in the Earth's crust, but silicate perovskites such as $MgSiO_3$ make up much of the mantle. From the point of view of magnetism, the mixed-valence manganites [7] have for long been of great interest. Much studied are the solid solutions between $La^{3+}Mn^{3+}O_3$ and $Sr^{2+}Mn^{4+}O_3$ or $Ca^{2+}Mn^{4+}O_3$, leading to mixed-valence compounds such as $La_{1-x}Sr_xMnO_3$. Each of the end members is antiferromagnetic

and insulating ($LaMnO_3$ is a canted antiferromagnet [7]), but the solid solutions may be ferromagnetic and conducting. Optimally doped $La_{1-x}Sr_xMnO_3$ with $x = 0.3$ is a half metal with the greatest Curie temperature of 380 K, and a rhombohedrally distorted perovskite structure. The substitution of Sr for La creates a mixture of $Mn^{4+}(t_{2g}{}^3)^{\uparrow}$ and $Mn^{3+}(t_{2g}{}^3e_g)^{\uparrow}$ on the B-sites of the structure [7] and the hopping $e_g{}^{\uparrow}$ electron mediates ferromagnetic coupling by double exchange. The ferromagnetic moment is consistently found to be slightly less than the 3.7_B, which would be expected if $(La_{0.7}Sr_{0.3})MnO_3$ were ideally half metallic, and it seems that both mobile $e_g{}^{\uparrow}$ electrons and immobile $t_{2g}{}^{\uparrow}$ electrons may be present at E_F. The compound is therefore classified as a transport half metal [54]. Residual resistivity is as low as $4 \times 10^{-7}\,\Omega\,m$, but a feature of the mixed-valence manganites is their colossal magnetoresistance. The resistivity may decrease by as much as 98% when a large field is applied close to T_C.

Elsewhere in the phase diagram, one can find different antiferromagnetic phases, and compounds that exhibit charge order and orbital order. There are other families of magnetic oxides with structures related to perovskite. These include the rare-earth orthoferrites $RFeO_3$ with an orthorhombic cell, which are antiferromagnets with Néel temperatures of 620–740 K. They form with all rare earths from La to Lu, and exhibit weak ferromagnetism with a moment of about $8\,kA\,m^{-1}$ owing to the Dzyaloshinkii–Moriya interaction. Other transition metals that form magnetically ordered perovskite-type materials are Ti, Cr, Co, and Ni. The possibilities for creating interesting solid solutions by substitution are almost endless but possibilities for practical applications are very limited because of the relatively low Curie temperatures. Cobalt in these materials is often found in a low-spin state, indicating that $\Delta > \mathcal{J}_H$.

Another big family are the double perovskites, which have a $(2, 2, 2)a_0$ cubic cell. Here a model compound is Sr_2FeMoO_6 (SFMO), which has a Curie temperature of 436 K [55]. The iron and molybdenum show NaCl-type order on the transition-metal sites of the perovskite lattice, and the single delocalized electron of the molybdenum mixes with the empty 3d states to provide strong ferromagnetic coupling among the iron spins. The moment is less than the $4\,\mu_B$ per formula expected for a stoichiometric half metal owing to Fe/Mo antisite defects.

1.5.7 CrO_2

Chromium dioxide has the tetragonal rutile structure, where the Cr^{4+} ions are octahedrally coordinated by oxygen [56]. It is the only binary oxide that is a ferromagnetic metal, with a Curie temperature of 396 K. Band structure calculations show that CrO_2 is a d-band half metal with a $\downarrow$ spin gap $\Delta^{\downarrow}$ of 0.5 eV in the minority-spin band. The conductivity at room temperature is $3 \times 10^5\,S\,m^{-1}$. The magnetization corresponds to an integral moment of 2.0_B per formula as expected for a half metal. Andreev reflection measurements on CrO_2 – superconductor point contacts give a spin polarization, $P \approx 90\%$ at temperatures of about 2 K [57]. Acicular CrO_2 powders were once used for magnetic video tapes.

Other magnetic rutile-structure oxides include VO_2, which is an antiferromagnet with a metal–insulator transition at 343 K [56].

1.5.8 $Tl_2Mn_2O_7$

The pyrochlore manganite $Tl_2Mn_2O_7$ is a cubic compound with an interesting electronic structure and unexpected magnetic properties [58]. There are eight formula units per unit cell. The Mn^{4+} ions are octahedrally coordinated by oxygen, and they form a corner-sharing tetrahedral array, similar to that of the B-sites in the spinel structure. In an ionic picture, the compound would be an insulator with Mn^{4+} ($3d^3$) and Tl^{3+} ($5d^{10}$) cations. Only the former bear a magnetic moment, $3\,\mu_B$, and they couple via Mn–O–Mn superexchange bonds. Antiferromagnetic Mn^{4+}–O–Mn^{4+} superexchange is highly frustrated by the three-membered rings of the tetrahedral array. The compound, however, is a ferromagnetic semimetal with $T_c = 118$ K and a small number of heavy holes at the top of a narrow band of mainly $t_{2g}{}^{\uparrow}$ character and an equal number of mobile electrons in a broad band of mixed Tl (6s), O (2p), and Mn (3d) character [59, 60]. The number of carriers has been estimated at 0.005 per manganese. The mobile electrons are expected to dominate the conduction, while the heavy holes will be easily localized by any impurities or disorder that may be present in the compound. $Tl_2Mn_2O_7$ can also be regarded as a half metal in so far as the heavy holes do not contribute significantly to the conduction.

More recently, the tetrahedral frustration in pyrochlore-structure compounds with rare earths has helped to develop the concept of *spin ice*. $Dy_2Ti_2O_7$ and $Ho_2Sn_2O_7$ are examples. The dysprosium has a [111] easy axis, and in each tetrahedron, the moments of two Dy^{3+} ions point inwards and two point outwards, analogous to hydrogen bonds in ice. Introducing defects in the frustrated lattice has the effect of creating widely separated positive and negative magnetic ''charges,'' which are free to move in the lattice. These have been described as magnetic ''monopoles,'' although they are always formed in pairs [61], and Maxwell's equation. $\nabla \cdot \boldsymbol{B} = 0$ is not violated!

1.6 Dilute Magnetic Oxides

A dilute magnetic oxide consists of a nonmagnetic oxide, such as those listed in Table 1.3, in which a small fraction of magnetic 3d cations has been introduced. The general formula of the oxide is MO_η, where η is an integer or rational fraction; so the formula of dilute magnetic oxide is

$$(M_{1-x}T_x)O_\eta$$

where $x < 10\%$. In view of our discussion of magnetic interactions in oxides in Section 1.4, we would not anticipate any long-range magnetic order in such a

material when x is below the percolation threshold x_p. The value of x_p is $\sim 2/Z_c$, where Z_c is the cation–cation coordination number; for example, Z_c is 12 for ZnO and 10 for TiO_2 (rutile), as may be seen from Figure 1.3.

A dilute two-dimensional lattice with $Z_c = 4$ is illustrated in Figure 1.15, where it can be seen that random occupancy leads to a distribution of isolated T ions, some nearest-neighbor pairs and a few larger clusters. The dimers and clusters are expected to couple antiferromagnetically, with a net moment for odd-membered clusters. When $x < 0.1$, the magnetic entities respond independently to an applied magnetic field, leading to a paramagnetic response that can be modeled approximately as a sum of Curie and Curie–Weiss terms

$$\chi = C_1/T + C_2/(T-\theta) \tag{1.22}$$

where C_1 and C_2 are Curie constants (Eq. (1.8)), and θ is negative with magnitude <100 K, representing the strength of a single antiferromagnetic exchange bond. The predicted paramagnetic behavior has been found in well-crystallized samples, for example, in Co-doped ZnO crystals where the Co^{2+} substitutes for Zn on tetrahedral sites, and $\theta = 65$ K [62].

Over the past 10 years, beginning with the 2001 Science report by Matsumoto *et al* [63] on thin films of Co-doped anatase TiO_2 produced by PLD, there has been a spate of reports of ferromagnetic-like behavior in thin films and nanocrystalline samples of dilute magnetic oxides. Most remarkably, the ferromagnetism is found at room temperature, and the corresponding Curie temperature must be >400 K. Table 1.6 reports some of the early results on various oxide systems [64]. It can be seen that they may be semiconducting (ZnO), insulating (TiO_2), or metallic ($(La,Sr)TiO_3$), and the effect is seen for a variety of 3d cations.

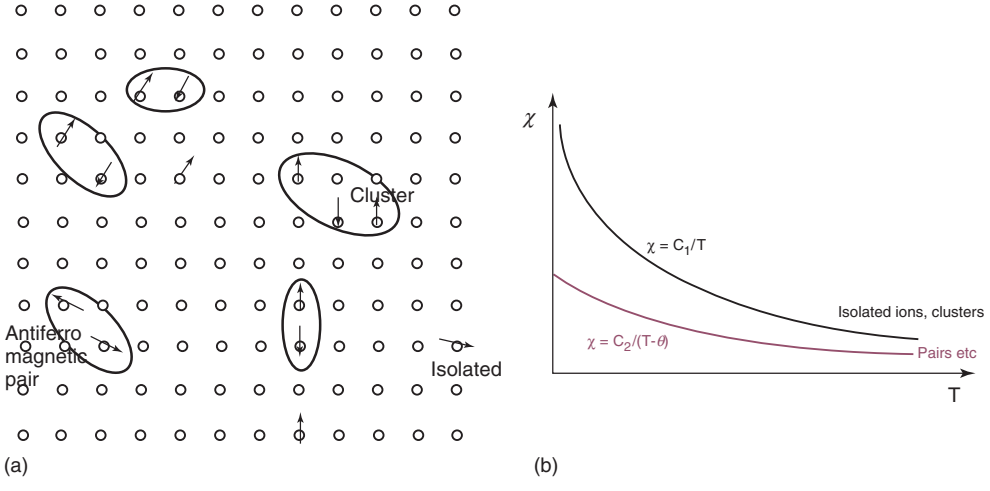

Figure 1.15 Dilute magnetic oxide below the percolation threshold. (a) Pairs and small clusters of magnetic ions are coupled by antiferromagnetic superexchange. (b) This leads to a paramagnetic susceptibility of the form given by Eq. 1.22.

Table 1.6 Reports of ferromagnetic oxide thin films with T_C above room temperature (Ref. [63]).

Material	E_g (eV)	Substitutions	Moment (μ_B) per 3d ion	T_C (K)
TiO_2	3.2	V – 5%	4.2	>400
		Co – 7%	0.3	>300
		Co – 1%–2%	1.4	>650
		Fe – 2%	2.4	300
SnO_2	3.5	Fe – 5%	1.8	610
		Co – 5%	7.5	650
ZnO	3.3	V – 15 %	0.5	>350
		Mn – 2.2%	0.16	>300
		Fe 5%,Cu 1%	0.75	550
		Co – 10%	2.0	280–300
		Ni – 0.9%	0.06	>300
CeO_2	2.0	Co – 3%	5.8	>750
In_2O_3	3.7	Fe – 5%	1.4	>600
		Cr – 2%	1.5	900
ITO	3.5	Mn – 5%	0.8	>400
$(La,Sr)TiO_3$	—	Co – 1.5%	2.5	550

The excitement engendered by these results was partly due to their quite unexpected nature, and partly because it was hoped that these films and related nanoparticles would turn out to be the long-anticipated room-temperature ferromagnetic semiconductors. The dilute magnetic oxides were thought to be *dilute magnetic semiconductors* (DMS). A DMS is a semiconducting material where 3d or 4f dopants order ferromagnetically under the influence of long-range exchange interactions to produce a uniform ferromagnetic state. The textbook example is $(Ga_{1-x}Mn_x)As$, where ferromagnetic ordering of Mn^{2+} ions occurs which occupy a level below the top of the As 4p valence band, with a value of T_C as high as 170 K for doping at the solubility limit $x = 0.07$ [65]. The material is magnetically homogeneous on the scale of a few nanometers [66].

The possibility of high-temperature ferromagnetism in ZnO doped with 5% of manganese was proposed by Dietl *et al.* [67]. The ferromagnetism was thought to be like that in (Ga,Mn)As, mediated by spin-polarized holes in the ligand p band. However, with the exception of ZnO, where the cations are in tetrahedral coordination and the bonding has significant covalent character with 2p holes that can exhibit reasonable mobility, oxides do not usually make good semiconductors. The carriers tend to be trapped and form small polarons owing to their Coulomb interaction with the oxygen anions. This is why many oxides may be off-stoichiometric, yet remain insulating.

There is a voluminous literature on the magnetic properties of dilute magnetic oxides, which is reviewed in subsequent chapters in this book. For doped ZnO

alone, there are over 1000 references in a recent review [68]. Here we restrict our discussion to just three points:

- The dilute magnetic oxides are not dilute magnetic semiconductors, as defined above.
- They are magnetically inhomogeneous, and only a small fraction of the volume is ferromagnetically ordered.
- The magnetism (when it is not due to impurity phases or experimental artifacts) is closely associated with defects in the material.

Some magnetization curves of thin films of dilute magnetic oxides are shown in Figure 1.16. What is remarkable about the data is that the curves are essentially anhysteretic and that they show very little temperature dependence between room temperature and 4 K. However, it should be emphasized that the superposition of curves obtained at different temperatures is achieved after correcting the data for a diamagnetic signal arising from the substrate, or from the oxide matrix in the case of bulk samples of nanoparticles. Since this cannot be precisely determined in the thin films it is normal practice to correct the data simply to give zero high-field slope which means that any temperature-dependent Curie law paramagnetism may be overlooked. However, the lack of temperature dependence of the nonlinear magnetization curves, like those in Figure. 1.16 entirely excludes the possibility of

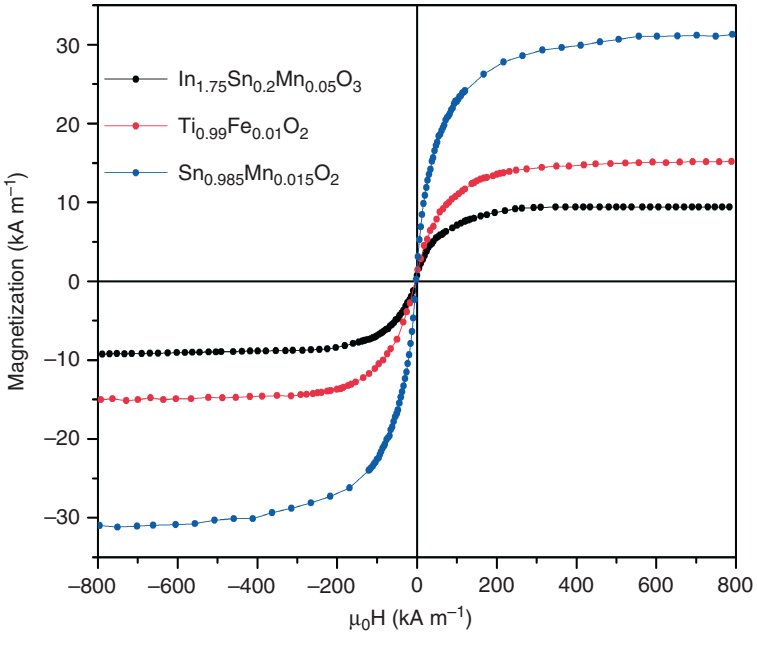

Figure 1.16 Some representative magnetization curves of thin film of dilute magnetic oxides.

superparamagnetism, for which the magnetization curves should superpose when M/M_s is plotted versus (H/T).

The first point is established by the observation that the dopant ions are not necessarily magnetically ordered when the sample is in its ferromagnetic state. The evidence includes (i) X-ray magnetic circular dichroism (XMCD) data on the cobalt in Co-doped ZnO [69], (ii) ^{57}Fe Mossbauer spectra of Fe-doped TiO_2 [70], and (iii) the Curie-law susceptibility observed for Mn in ITO and other dilute oxides when the data are not corrected to give zero high-field slope at each temperature [71]. All these measurements indicate that most, if not all, of the dopant ions remain *paramagnetic* down to liquid-helium temperatures, as expected from Eq. 1.22. The practice that we followed in Table 1.6 of relating the moment to the dopant, quoting it, for example, as $2.0\,\mu_B$ per Co ion is therefore misleading because it is not necessarily the 3d dopant that is ferromagnetically ordered. In fact, evidence that this approach was mistaken emerged quite early on, when moments per dopant exceeding the greatest possible spin-only value began to be reported, especially in lightly-doped material [72–75].

The second point can be inferred from the magnetization curves. If the samples were uniformly magnetized on a microscopic scale, as we expect for a DMS, the very small value of the magnetization ($\approx 10\,\mathrm{kA\,m^{-1}}$ in thin films or $\approx 10\,\mathrm{A\,m^{-1}}$ in nanoparticles) should give rise to a large value of the anisotropy field, even in cubic materials, and therefore produce substantial coercivity. Such coercivity, in excess of $100\,\mathrm{kA\,m^{-1}}$, is observed in powders of rare-earth garnets near their compensation temperature (Figure 1.14). These materials exhibit a magnetization of $1–10\,\mathrm{kA\,m^{-1}}$, similar to that of the dilute magnetic oxides, yet no coercivity is found in the latter and thus we infer that they are unlikely to be uniformly magnetized.

Another serious problem with the idea that dilute magnetic oxides are homogeneously magnetized dilute ferromagnetic semiconductors is the high value of the Curie temperature. Few insulating oxides are ferromagnetic; they usually order antiferromagnetically or ferrimagnetically on account of the antiferromagnetic superexchange. Furthermore, very few oxides order magnetically above 1000 K, and nothing is known to have a higher Curie temperature than cobalt (1360 K). It stretches the imagination to believe that a material with 5% of magnetic ions could have a Curie temperature much above 400 K. The magnetic energy density varies as x or $\sqrt{x}$; so these high Curie temperatures cannot be achieved with uniformly magnetized material [64].

We can, however, do better, and estimate the volume fraction that is magnetically ordered from magnetization curves like those in Figure 1.16 [76]. The analysis is based on a comparison of the average magnetization of the sample M_s deduced directly as the saturation magnetization, with the magnetization of the ferromagnetic regions M_f deduced from the field H_0 obtained by extrapolating the slope of the magnetization curve at the origin to saturation. The argument is that the approach to saturation must be governed by dipolar interactions rather than by magnetocrystalline anisotropy – if magnetocrystalline anisotropy were involved, there would be a clear temperature dependence of the magnetization curves and

eventual appearance of coercivity at low temperature. In fact the magnetization curves are practically anhysteretic, and show almost no temperature dependence between 4 K and room temperature. H_0 therefore represents the average magnitude of the demagnetizing field $H_0 = -\mathcal{N}M_f$, where the demagnetizing factor $\mathcal{N}$ is a number between 0 and 1, and M_f is the magnetization of the ferromagnetic regions. Often, there is little dependence of the magnetization on the field direction with respect to the plane of the film; so it is reasonable to take $\mathcal{N} \approx 1/3$, but the exact value is unimportant for our argument. We therefore deduce from the values of H_0 for the curves in Figure 1.16 that M_f is $\sim$400 kA m^{-1} and M_s $\sim$20 kAm^{-1}. The ferromagnetic volume fraction in the films $f = M_s/M_f$ is therefore *only a few percent*. Applying the same argument to data on nanoparticles gives values that are much lower. Figure 1.17 is a scatter plot of very many samples of dilute and undoped magnetic oxides and nanoparticles.

The view that the magnetism is confined to a small portion of the sample volume is supported by the absence of any ferromagnetism in well-crystallized samples of dilute magnetic oxides [62, 77], and its appearance after treatments such as heating the sample under vacuum, which has the effect of creating defects and modifying the oxygen stoichiometry. Contamination of the samples by small quantities of ferromagnetic impurities such as iron or magnetite is sometimes a problem, and there are well-documented accounts of the perils that can arise when scrupulous care is not observed in the experiments and appropriate blank samples are not examined [78, 79]. The presence of such impurities may be flagged by the values of M_f. In systems such as Co-doped ZnO, the cobalt has a tendency to form dispersed cobalt nanoparticles, which are ferromagnetic [80]. It has been a bane that the lack of reproducibility of many of the results from different laboratories, and even

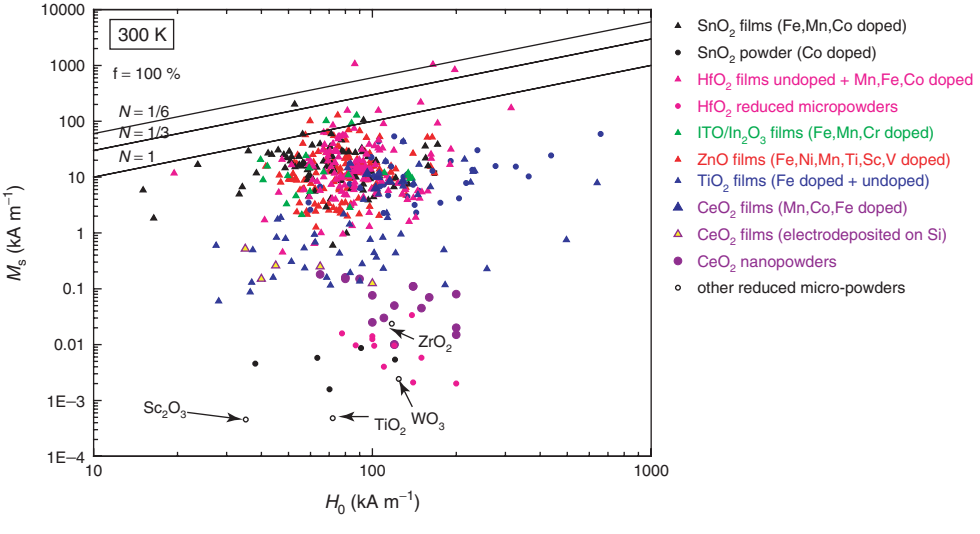

Figure 1.17 Compilation of data for thin film and nanoparticulate systems showing the correlation between M_s and H_0 for different classes of material.

within the same laboratory, compounded by the fact that the magnetization of certain samples is found to decay with time [81]. The problems may be remedied by better control of the deposition conditions, for example, by electrochemical growth of oxides where the magnetic moment appears in a narrow range of conditions [82].

A defect-related origin of the ferromagnetism is supported by its observation in some samples of *undoped* material. These include films of HfO_2 [83, 84], ZnO[85, 86], TiO_2 [87], and In_2O_3 [74]. This phenomenon is known as d^0 *magnetism* [88], and it reinforces the idea that defects are necessary, but 3d dopants are not essential.

In order to arrive at a satisfactory explanation of the magnetic behavior of dilute magnetic oxides and d^0 systems, it is necessary to tie down the relevant defect structure. This is a challenge, as it is difficult to characterize and quantify unknown defects in solids, especially in thin films. There is an area where electronic structure calculations can help. The obvious places to look in a thin film are the surface, the interface with the substrate and the grain boundaries. For nanocrystalline material, a significant fraction of the atoms are at the surface or in grain boundaries. Evidence for a correlation between magnetism and grain size gas been reported for ZnO nanocrystallites [89]. Extended defects seem to be a more likely source of percolating magnetism than point defects.

The influence of defects on magnetism has been modeled in terms of a narrow, spin-split defect-related impurity band [90]. This has been shown to lead to a high Curie temperature, as spin-wave excitations are suppressed in the half-metallic band. This Stoner model of the magnetism, involving a small fraction of the sample volume, contrasts with the Heisenberg model used to treat the magnetism of ions with local moments in Section 1.4. Transition-metal dopants may nonetheless play a role, but as a reservoir of charge for the impurity band. When the ions exist in different charge states, they can help to ensure filling to the point where the Stoner criterion is satisfied. This phenomenon is known as *charge transfer ferromagnetism* [91]. Models for the magnetism of dilute magnetic oxides are discussed in Ref. [92].

A quite different and more speculative explanation is based on the suggestion that the moment is essentially of orbital origin, and that the electrons moving on the surface of a particle, or around a continuous grain boundary can develop a giant orbital moment, with giant paramagnetic susceptibility [93].

1.6.1
Magnetism of Oxide Surfaces, Interfaces, and Defects

There are inevitable changes in electronic structure at defects in crystals. The symmetry is lowered at the surface, or at the interface with a substrate. The surface may be charged or uncharged depending on the termination of plane involved. For example, the 001 surface of TiO_2 may present a plane of negatively charged oxygen or positively charged titanium ions. The reduced number of neighbors at the surface can produce band narrowing and localization. There are suggestions that the surfaces of some nonmagnetic oxides might even support magnetic order [94].

Some direct evidence that defects can lead to the weak high-temperature magnetism that we have been discussing is provided by experiments irradiating single

crystals of TiO_2 [95], which show that the appearance of magnetism is associated with the tracks of radiation damage.

There are numerous calculations of the electronic structure of point defects in various kinds of oxides. A key parameter is the relative energy of singly and doubly-occupied defects. A single electron necessarily has an unpaired spin, but if the energy U needed to add a second electron is negative, the defects will tend to be unoccupied or occupied by two electrons with paired spins in an s-like orbital. The system is then nonmagnetic. However, if U is positive and the average electron occupancy of the defects is somewhat greater than one, the extra electrons may be delocalized and produce ferromagnetic coupling of the core spins. For example, a missing pair of Zn and O ions in ZnO might be a defect with this property [96].

Turning to extended defects, a very interesting model system is the planar interface between (001) $LaAlO_3$ and $SrTiO_3$, illustrated in Figure 1.18. Each oxide has a perovskite-type structure; the structure of $LaAlO_3$ may be considered as a sequence of alternating polar planes of $(LaO)^+$ and $(AlO_2)^-$, whereas that of $SrTiO_3$ consists of alternating charge-neutral planes of (SrO) and (TiO_2). The planar interface reconstructs to transfer 0.5 electron per interfacial unit cell into the empty Ti 3d band close to the interface, giving an electron density of $3 \times 10^{18}\ m^{-2}$ [94]. The properties of the two-dimensional electron gas at the interface are quite unusual. There is a tendency toward phase segregation into ferromagnetic and superconducting regions [97]. The first evidence for magnetic order was indirect, from magnetoresistance measurements [98], but recent experiments have shown evidence of magnetization corresponding to magnetic moments of order $1\,\mu_B$ per unit cell persisting up to room temperature, and superconductivity below 60 K [99]. Analysis of the magnetization curve, assuming $\mathcal{N} = 1/3$ for the ferromagnetic regions, yields a thickness of the ferromagnetic interface of order 1 nm, or three unit cells.

The recent work on oxide–oxide interfaces demonstrates that they can show electronic properties completely different from that of either constituent, including room-temperature ferromagnetism. By gating, it is possible to control the properties

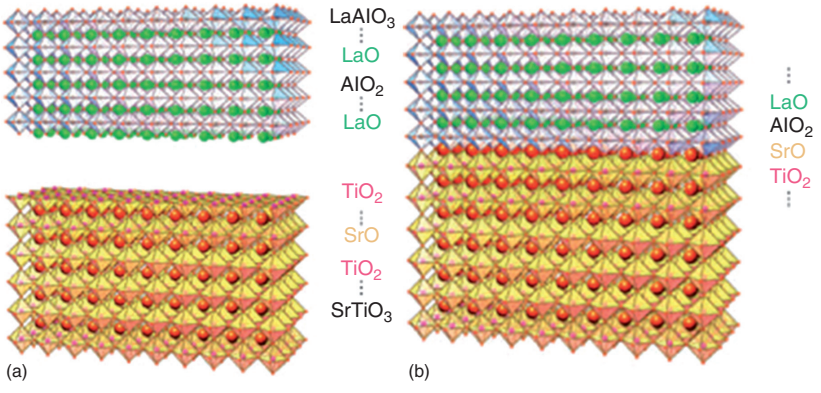

Figure 1.18 (a) Schematic of a TiO_2-terminated (001) $SrTiO_3$ single crystal before contact with an epitaxial $LaAlO_3$ overlayer. (b) Epitaxial $LaAlO_3$ on TiO_2-terminated $SrTiO_3$.

with an external electric field [100]. The results encourage a more systematic investigation of well-defined oxide interfaces in a quest to understand better the properties of dilute magnetic oxides and d^0 magnetism.

1.7 Conclusions

This introduction to magnetic oxides provides a background to subsequent chapters in the first half of the book. While the magnetic properties of concentrated magnetic oxides, and well-crystallized, paramagnetic dilute magnetic oxides are now well-understood, the magnetism of defective dilute magnetic oxides, d^0 magnets, and oxide–oxide interfaces is not. There are areas where new physics and materials science may emerge, as well as possible applications enabled by the high Curie temperature.

Acknowledgments

This work was supported by Science Foundation Ireland as part of the NISE project, contract number 10/INI/I3002.

References

1. Kloss, A. (1994) *Geschichte des Magnetismus*, VDE-Verlag, Berlin.
2. Blackman, M. (1983) The lodestone: a survey of the history and the physics. *Contemp. Phys.*, **24**, 319.
3. Dunlop, D.J. and Özdemir, Ö. (1997) *Rock Magnetism: Fundamentals and Frontiers*, Cambridge University Press, New York.
4. Kurti, N. and Néel, L. (1988) *Selected Works of Louis Néel*, Gordon and Breach, New York.
5. Wijn, H.P.J. and Smit, J. (1959) *Ferrites: Physical Properties of Ferrimagnetic Oxides in Relation to their Technical Applications*, John Wiley & Sons, Inc., New York.
6. Goodenough, J.B. (1963) *Magnetism and the Chemical Bond*, Wiley Interscience, New York.
7. Coey, J.M.D., Viret, M., and Von Molnar, S. (1999) Mixed-valence manganites. *Adv. Phys.*, **48**, 167.
8. Ogale, S.B. (2005) *Thin Films and Heterostructures for Oxide Electronics*, Springer, Berlin.
9. Dionne, G.F. (2009) *Magnetic Oxides*, Springer.
10. Craik, D.J. (1975) *Magnetic Oxides*, John Wiley & Sons, Inc., New York.
11. Coey, J.M.D. (2010) *Magnetism and Magnetic Materials*, Cambridge University Press, Cambridge.
12. Catlow, C.R.A. and Stoneham, A.M. (1981) Defect equilibria in transition metal oxides. *J. Am. Ceram. Soc.*, **64**, 234.
13. Zaanen, J., Sawatzky, G.A., and Allen, J.W. (1985) Band gaps and electronic structure of transition-metal compounds. *Phys. Rev. Lett.*, **55**, 418.
14. Burns, R.G. (1993) *Mineralogical Applications of Crystal Field Theory*, Cambridge University Press, Cambridge.
15. Patnaik, P. (2004) *Dean's Analytical Chemistry Handbook*, McGraw-Hill, New York.

16. Brinker, C.J. and Scherer, G.W. (1990) *Sol–Gel Science: the Physics and Chemistry of Sol–Gel Processing*, Academic Press.
17. West, A.R. (2007) *Solid State Chemistry and its Applications*, Wiley India.
18. Patil, K.C., Aruna, S.T., and Ekambaram, S. (1997) Combustion synthesis. *Curr. Opin. Solid State Mater. Sci.*, **2**, 158.
19. Scheel, H.J. (2000) Historical aspects of crystal growth technology. *J. Cryst. Growth*, **211**, 1.
20. Karas, G.V. (2005) *New Developments in Crystal Growth Research*, Nova Science Publication Inc., New York.
21. Brandle, C.D. (2004) Czochralski growth of oxides. *J. Cryst. Growth*, **264**, 593.
22. Balbashov, A.M. and Egorov, S.K. (1981) Apparatus for growth of single crystals of oxide compounds by floating zone melting with radiation heating. *J. Cryst. Growth*, **52**, 498.
23. Berthon, J., Revcolevschi, A., Morikawa, H. *et al.* (1979) Growth of wustite ($Fe_{1-x}O$) crystals of various stoichiometries. *J. Cryst. Growth*, **47**, 736.
24. Robertson, J.M. (1974) Growth of oxide single crystals–use and care of platinum apparatus. *Platinum Met. Rev.*, **18**, 15.
25. Scheafer, H. (1964) *Chemical Transport Reactions*, Academic Press, New York.
26. Ziese, M. and Thornton, M.J. (2001) *Spin Electronics*, Springer-Verlag, Berlin.
27. Sze, S.M. (2009) *Semiconductor Devices: Physics and Technology*, Wiley, New Delhi, India.
28. Hill, R.J. (1986) *Physical Vapour Deposition*, 2nd edn, Berkeley, CA.
29. Cho, A.Y. and Arthur, J.R. (1975) Molecular beam epitaxy. *Prog. Solid State Chem.*, **10**, 157.
30. Howson, R.P. and Ridge, M.I. (1981) Deposition of transparent heat-reflecting coatings of metal oxides using reactive planar magnetron sputtering of a metal and/or alloy. *Thin Solid Films*, **77**, 119.
31. Dijkkamp, D., Venkatesan, T., Wu, X.D. *et al.* (1987) Preparation of Y-Ba-Cu oxide superconductor thin films using pulsed laser evaporation from high Tc bulk material. *Appl. Phys. Lett.*, **51**, 619.
32. George, S.M. (2010) Atomic layer deposition: an overview. *Polymer*, **1550**, 125.
33. Burns, R.G. (1981) Intervalence transitions in mixed-valence minerals of iron and titanium. *Annu. Rev. Earth Planet. Sci.*, **9**, 345.
34. Chamritski, I. and Burns, G. (2005) Infrared- and Raman-active phonons of magnetite, maghemite, and hematite: a computer simulation and spectroscopic study. *J. Phys. Chem. B*, **109**, 4965.
35. Khomskii, D.I. and Sawatzky, G.A. (1997) Interplay between spin, charge and orbital degrees of freedom in magnetic oxides. *Solid State Commun.*, **102**, 87.
36. Ballhausen, C.J. and Gray, H.B. (1962) The electronic structure of the vanadyl ion. *Inorg. Chem.*, **1**, 111.
37. Hutchings, M.T. and Ray, D.K. (1963) Investigation into the origin of crystalline electric field effects on rare earth ions: I. Contribution from neighbouring induced moments. *Proc. Phys. Soc.*, **81**, 663.
38. Anderson, P.W. (1950) Antiferromagnetism. Theory of superexchange interaction. *Phys. Rev.*, **79**, 350.
39. Anderson, P.W. and Hasegawa, H. (1955) Considerations on double exchange. *Phys. Rev.*, **100**, 675.
40. Nolting, W. and Ramakanth, A. (2009) *Quantum Theory of Magnetism*, Springer-Verlag, Berlin.
41. Coey, J.M.D. and Venkatesan, M. (2002) Half-metallic ferromagnetism: example of CrO_2. *J. Appl. Phys.*, **91**, 8345.
42. Tokura, Y. and Nagaosa, N. (2000) Orbital physics in transition-metal oxides. *Science*, **288**, 462.
43. Feng, D. and Jin, G. (2005) *Introduction to Condensed Matter Physics*, World Scientific.
44. Senn, M.S., Wright, J.P., and Attfield, J.P. (2012) Charge order and three-site distortions in the verwey structure of magnetite. *Nature*, **481**, 873.
45. Morrish, A.H. (1994) *Canted Antiferromagnetism: Hematite*, World Scientific, Singapore.
46. Artman, J.O., Murphy, J.C., and Foner, S. (1965) Magnetic anisotropy in antiferromagnetic corundum-type sesquioxides. *Phys. Rev.*, **138**, A912.

47. Zhang, Z. and Satpathy, S. (1991) Electron states, magnetism, and the Verwey transition in magnetite. *Phys. Rev. B*, **44**, 13319.
48. Wohlfarth, E.P. and Buschow, K.H.J. (1980) *Ferromagnetic Materials: A Handbook on the Properties of Magnetically Ordered Substances*, North Holland, Amsterdam.
49. (a) Verwey, E.J.W. (1939) Electronic conduction of magnetite (Fe_3O_4) and its transition point at low temperatures. *Nature*, **144**, 327. (b) Verwey, E.J.W. and Haayman, P.W. (1941) Electronic conductivity and transition point of magnetite. *Physica*, **8**, 979.
50. Kuneš, J., Anisimov, V.I., Skornyakov, S.L. *et al.* (2007) NiO: correlated band structure of a charge-transfer insulator. *Phys. Rev. Lett.*, **99**, 156404.
51. Morin, F.J. (1959) Oxides which show a metal-to-insulator transition at the Neel temperature. *Phys. Rev. Lett.*, **3**, 34.
52. Gilleo, M.A. and Wohlfarth, E.P. (1980) Ferromagnetic insulators: garnets, in *Ferromagnetic Materials: A Handbook on the Properties of Magnetically Ordered Substances*, Vol. 2 Chapter 1, North Holland, Amsterdam.
53. Stäblein, H. (1982) *Handbook of Ferromagnetic Materials*, Vol. 3, North Holland, Amsterdam, p. 441.
54. Nadgorny, B., Mazin, I.I., Osofsky, M. *et al.* (2001) Origin of high transport spin polarization in $La_{0.7}Sr_{0.3}MnO_3$:direct evidence for minority spin states. *Phys. Rev. B*, **63**, 184433.
55. Kobayashi, K.I., Kimura, T., Sawada, H. *et al.* (1998) Room-temperature magnetoresistance in an oxide material with an ordered double-perovskite structure. *Nature*, **395**, 677.
56. Chamberland, B.L. (1977) The chemical and physical properties of CrO_2 and tetravalent chromium oxide derivatives. *Crit. Rev. Solid State Mater. Sci.*, **7**, 1.
57. Soulen, R.J., Byers, J.M., Osofsky, M.S. *et al.* (1998) Measuring the spin polarization of a metal with a superconducting point contact. *Science*, **282**, 85.
58. Shimakawa, Y., Kubo, Y., and Manako, T. (1996) Giant magnetoresistance in $Ti_2Mn_2O_7$ with the pyrochlore structure. *Nature*, **379**, 53–55.
59. Singh, D.J. (1997) Magnetoelectronic effects in pyrochlore $Tl_2Mn_2O_7$: role of Tl-O covalency. *Phys. Rev. B*, **55**, 313.
60. Imai, H., Shimakawa, Y., Sushko, Y.V. *et al.* (2000) Carrier density change in the colossal-magnetoresistance pyrochlore $Tl_2Mn_2O_7$. *Phys. Rev. B*, **62**, 12190.
61. Castelnovo, C., Moessner, R., and Sondhi, S.L. (2008) Magnetic monopoles in spin ice. *Nature*, **451**, 42.
62. Rao, C.N.R. and Deepak, F.L. (2004) Absence of ferromagnetism in Mn-and Co-doped ZnO. *J. Mater. Chem.*, **15**, 573.
63. Matsumoto, Y., Murakami, M., Shono, T. *et al.* (2001) Room-temperature ferromagnetism in transparent transition metal-doped titanium dioxide. *Science*, **291**, 854.
64. Coey, J.M.D. and Chambers, S.A. (2008) Oxide dilute magnetic semiconductors–fact or fiction? *MRS Bull.*, **33**, 1053.
65. Jungwirth, T., Wang, K.Y., Mašek, J. *et al.* (2005) Prospects for high temperature ferromagnetism in (Ga, Mn) as semiconductors. *Phys. Rev. B*, **72**, 165204.
66. Dunsiger, S.R., Carlo, J.P., Goko, T. *et al.* (2010) Spatially homogeneous ferromagnetism of (Ga, Mn) as. *Nat. Mater.*, **9**, 299.
67. Dietl, T., Ohno, H., Matsukura, F. *et al.* (2000) Zener model description of ferromagnetism in zinc-blende magnetic semiconductors. *Science*, **287**, 1019.
68. Pan, F., Song, C., Liu, X.J. *et al.* (2008) Ferromagnetism and possible application in spintronics of transition-metal-doped ZnO films. *Mater. Sci. Eng., R*, **62**, 1.
69. Tietze, T., Gacic, M., Schütz, G. *et al.* (2008) XMCD studies on Co and Li doped ZnO magnetic semiconductors. *New J. Phys.*, **10**, 055009.
70. Coey, J.M.D., Stamenov, P., Gunning, R.D. *et al.* (2010) Ferromagnetism in defect-ridden oxides and related materials. *New J. Phys.*, **12**, 053025.

71. Venkatesan, M., Gunning, R.D., Stamenov, P. *et al.* (2008) Room temperature ferromagnetism in Mn- and Fe-doped indium tin oxide thin films. *J. Appl. Phys.*, **103**, 07D135.
72. Ogale, S.B., Choudhary, R.J., Buban, J.P. *et al.* (2003) High temperature ferromagnetism with a giant magnetic moment in transparent Co-doped $SnO_{2-\delta}$. *Phys. Rev. Lett.*, **91**, 77205.
73. Venkatesan, M., Fitzgerald, C.B., Lunney, J.G. *et al.* (2004) Anisotropic ferromagnetism in substituted zinc oxide. *Phys. Rev. Lett.*, **93**, 177206.
74. Hong, N.H., Sakai, J., Poirot, N. *et al.* (2006) Room-temperature ferromagnetism observed in undoped semiconducting and insulating oxide thin films. *Phys. Rev. B*, **73**, 132404.
75. Fitzgerald, C.B., Venkatesan, M., Dorneles, L.S. *et al.* (2006) Magnetism in dilute magnetic oxide thin films based on SnO_2. *Phys. Rev. B*, **74**, 115307.
76. Coey, J.M.D., Mlack, J.T., Venkatesan, M. *et al.* (2010) Magnetization process in dilute magnetic oxides. *IEEE Trans. Magn.*, **46**, 2501.
77. Ney, A., Ollefs, K., Ye, S. *et al.* (2008) Absence of intrinsic ferromagnetic interactions of isolated and paired Co dopant atoms in $Zn_{1-x}Co_xO$ with high structural perfection. *Phys. Rev. Lett.*, **100**, 157201.
78. Grace, P.J., Venkatesan, M., Alaria, J. *et al.* (2009) The origin of the magnetism of etched silicon. *Adv. Mater.*, **21**, 71.
79. García, M.A., Fernández Pinel, E., De la Venta, J. *et al.* (2009) Sources of experimental errors in the observation of nanoscale magnetism. *J. Appl. Phys.*, **105**, 013925.
80. Dorneles, L.S., Venkatesan, M., Gunning, R. *et al.* (2007) Magnetic and structural properties of Co-doped ZnO thin films. *J. Magn. Magn. Mater.*, **310**, 2087.
81. Zukova, A., Teiserskis, A., van Dijken, S. *et al.* (2006) Giant moment and magnetic anisotropy in Co-doped ZnO films grown by pulse-injection metal organic chemical vapor deposition. *Appl. Phys. Lett.*, **89**, 232503.
82. Ackland, K., Monzon, L.M.A., Venkatesan, M. *et al.* (2011) Magnetism of nanostructured CeO_2. *IEEE Trans. Magn.*, **47**, 3509.
83. Venkatesan, M., Fitzgerald, C.B., and Coey, J.M.D. (2004) Thin films: unexpected magnetism in a dielectric oxide. *Nature*, **430**, 630.
84. Ran, J. and Yan, Z. (2009) Observation of ferromagnetism in highly oxygen-deficient HfO_2 films. *J. Semicond.*, **30**, 102002.
85. Zhang, Y. and Xie, E. (2010) Nature of room-temperature ferromagnetism from undoped ZnO nanoparticles. *Appl. Phys. A*, **99**, 955.
86. Mal, S., Nori, S., Jin, C. *et al.* (2010) Reversible room temperature ferromagnetism in undoped zinc oxide: correlation between defects and physical properties. *J. Appl. Phys.*, **108**, 073510.
87. Yoon, S.D., Chen, Y., Yang, A. *et al.* (2006) Oxygen-defect-induced magnetism to 880 K in semiconducting anatase $TiO_{2-\delta}$ films. *J. Phys. Condens. Matter*, **18**, L355.
88. Coey, J.M.D. (2005) d^0 ferromagnetism. *Solid State Sci.*, **7**, 660.
89. Straumal, B.B., Mazilkin, A.A., Protasova, S.G. *et al.* (2009) Magnetization study of nanograined pure and Mn-doped ZnO films: formation of a ferromagnetic grain-boundary foam. *Phys. Rev. B*, **79**, 205206.
90. Edwards, D.M. and Katsnelson, M.I. (2006) High-temperature ferromagnetism of sp electrons in narrow impurity bands: application to CaB_6. *J. Phys. Condens. Matter*, **18**, 7209.
91. Coey, J.M.D., Wongsaprom, K., Alaria, J. *et al.* (2008) Charge-transfer ferromagnetism in oxide nanoparticles. *J. Phys. D: Appl. Phys.*, **41**, 134012.
92. Evegeny, Y.T., Tsymbal, E.Y., and Zutic, I. (2010) *Spin Transport and Magnetism in Electronic Systems*, Taylor and Francis.
93. Hernando, A., Crespo, P., and Garcia, M.A. (2006) Origin of orbital ferromagnetism and giant magnetic anisotropy at the nanoscale. *Phys. Rev. Lett.*, **96**, 57206.

94. Millis, A.J. (2011) Moment of magnetism. *Nat. Phys.*, **7**, 749.

95. Zhou, S., Čižmár, E., Potzger, K. *et al.* (2009) Origin of magnetic moments in defective TiO_2 single crystals. *Phys. Rev. B*, **79**, 113201.

96. Chakrabarty, A. and Patterson, C.H. (2011) Defect-trapped electrons and ferromagnetic exchange in ZnO. *Phys. Rev. B*, **84**, 054441.

97. Bert, J.A., Kalisky, B., Bell, C. *et al.* (2011) Direct imaging of the coexistence of ferromagnetism and superconductivity at the $LaAlO_3/SrTiO_3$ interface. *Nat. Phys.*, **7**, 767.

98. Brinkman, A., Huijben, M., Van Zalk, M. *et al.* (2007) Magnetic effects at the interface between non-magnetic oxides. *Nat. Mater.*, **6**, 493.

99. Ariando , Wang, X., Baskaran, G., and Liu, Z.Q. (2011) Electronic phase separation at the $LaAlO_3/SrTiO_3$ interface. *Nat. Commun.*, **2**, 188.

100. Caviglia, A.D., Gariglio, S., Reyren, N. *et al.* (2008) Electric field control of the $LaAlO_3/SrTiO_3$ interface ground state. *Nature*, **456**, 624.